RL-TR-93-84
In-House Report
May 1993

TRUE TIME DELAY OPTICALLY CONTROLLED DUAL BAND TRANSMITTER

Serey Thai

APPROVED FOR PUBLIC RELEASE; DISTRIBUTION UNLIMITED.

Rome Laboratory
Air Force Materiel Command
Griffiss Air Force Base, New York

This report has been reviewed by the Rome Laboratory Public Affairs Office (PA) and is releasable to the National Technical Information Service (NTIS). At NTIS it will be releasable to the general public, including foreign nations.

RL-TR-93-84 has been reviewed and is approved for publication.

APPROVED: 

DANIEL J. McAULIFFE, Chief
Telecommunications Division
Command, Control, & Communications Directorate

FOR THE COMMANDER: 

JOHN A. GRANIERO
Chief Scientist
Command, Control, & Communications Directorate

If your address has changed or if you wish to be removed from the Rome Laboratory mailing list, or if the addressee is no longer employed by your organization, please notify RL (C3DB) Griffiss AFB NY 13441-5700. This will assist us in maintaining a current mailing list.

Do not return copies of this report unless contractual obligations or notices on a specific document require that it be returned.

REPORT DOCUMENTATION PAGE

Form Approved
OMB No. 0704-0188

1. AGENCY USE ONLY (Leave Blank)	2. REPORT DATE	3. REPORT TYPE AND DATES COVERED
	May 1993	In-House Feb 92 - Dec 92

4. TITLE AND SUBTITLE
TRUE TIME DELAY OPTICALLY CONTROLLED DUAL BAND TRANSMITTER

5. FUNDING NUMBERS
PE - 62702F
PR - 4519
TA - 21
WU - 88

6. AUTHOR(S)
Serey Thai

7. PERFORMING ORGANIZATION NAME(S) AND ADDRESS(ES)
Rome Laboratory (C3DB)
525 Brooks Road
Griffiss AFB NY 13441-4505

8. PERFORMING ORGANIZATION REPORT NUMBER
RL-TR-93-84

9. SPONSORING/MONITORING AGENCY NAME(S) AND ADDRESS(ES)
Rome Laboratory (C3DB)
525 Brooks Road
Griffiss AFB NY 13441-4505

10. SPONSORING/MONITORING AGENCY REPORT NUMBER

11. SUPPLEMENTARY NOTES
Rome Laboratory Project Engineer: Serey Thai/C3DB (315) 330-7457

12a. DISTRIBUTION/AVAILABILITY STATEMENT
Approved for public release; distribution unlimited.

12b. DISTRIBUTION CODE

13. ABSTRACT (Maximum 200 words)

The main principal of this microwave multiband phased array antenna is the use of optically controlled photonic delay line for beam forming and steering. This system is suitable for spaceborne and airborne phased array applications. It also has a potential to perform frequency hopping of transmitting signals since it is a dual band transmitter (L and X-band) and the dual band system is controlled by one set of frequency independent delay lines. The L-band (1 to 2.6 GHz) array and the X-band (8 to 12 HGz) array, each has the same physical length. Each is split into four subarrays and use a common time delay generator for each subarray on both bands. True time delay with wideband radiating elements permits large transmit and receive frequency excursions without beam wander (beam squint) as the frequency is changed, and also permits the use of wideband waveforms. The advantage also extends to both communications and surveillance applications where the beam wanders off target could occur without the use of the optically controlled true time delay beam forming and steering.

14. SUBJECT TERMS
optical control, phased array antenna, microwave optics, photonics

15. NUMBER OF PAGES
48

16. PRICE CODE

17. SECURITY CLASSIFICATION OF REPORT	18. SECURITY CLASSIFICATION OF THIS PAGE	19. SECURITY CLASSIFICATION OF ABSTRACT	20. LIMITATION OF ABSTRACT
UNCLASSIFIED	UNCLASSIFIED	UNCLASSIFIED	U/L

TABLE OF CONTENTS

SECTIONS

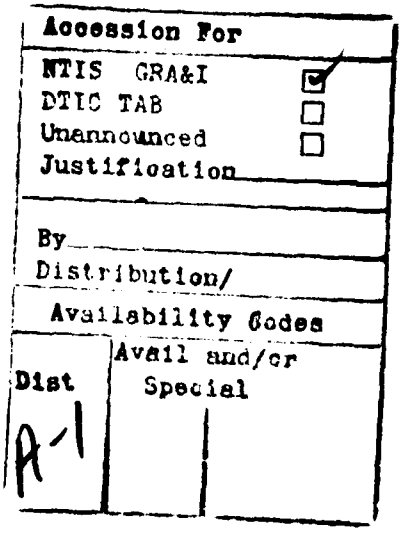

TWO BAND OPTICALLY CONTROLLED PHASED ARRAY

2 BAND OPTICAL BEAM CONTROL ARRAY

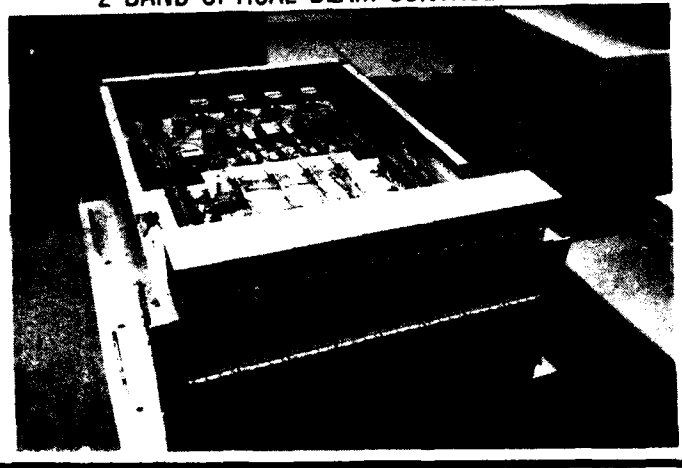

- FREQUENCIES 1.8-2.0GHZ (L-BAND)
  9.5-10.5GHZ (X-BAND)
- SCAN ±28° LINEAR
- STEPSIZE 4°
- NUMBER OF SUBARRAYS 4
- L-BAND 2 ELEMENTS/SUBARRAY
- X-BAND 8 ELEMENTS/SUBARRAY
- ARRAY LENGTH 21 INCHES
- 3 BIT TIME DELAY NETWORK

ADVANTAGE

- TRUE TIME DELAY
  - FREQUENCY INDEPENDENT
  - COMMON OPTICAL TIME DELAY NETWORK FOR SUBARRAY STEERING, BOTH BANDS
- NO BEAM SQUINT
- AUTOMATIC CONTROL

1.0 INTRODUCTION

The main principle of this microwave multiband phased array antenna is the use of optically controlled photonic delay lines for beam forming and steering. The use of fiber optic delay lines in the phased array antenna instead of phase shifters, RF waveguide, or coaxial cable has the following advantages: light weight, compactability, flexibility, wide band operation, nondispersive over multiple bands of microwave frequencies, and immunity to electromagnetic interference. This system is also suitable for spaceborne and airborne phased array applications. It has the potential to perform frequency hopping of transmitting signals since it is a dual band transmitter (L and X-band) and the dual band system is controlled by one set of delay lines. The L-band (1 to 2.6 GHz) array and the X-band (8 to 12 GHz) array, each has the same physical length. Each is split into four subarrays and use a common time delay generator for each subarray on both bands.

The advantages of true time delay RF beam forming and beam steering are well known. True time delay with wideband radiating elements permits large transmit and receive frequency excursions without beam wander (beam squint) as the frequency is changed, and also permits the use of wideband waveforms. This report reveals how far-field patterns verify near-field pattern generation and that true time delay beam pointing does not significantly change with frequency.

The near-field and far-field pattern development is under sponsorship of Rome Laboratory (formerly Rome Air Development Center). Hughes Aircraft Company developed the two-band Optically Controlled Phased Array Transmitter under contract to Rome Laboratory. The content of this paper is devoted to understanding the function of the transmitter and results of beam pattern development. These tasks are accomplished as follows : **a)** Develop the theory that led to the design, **b)** Analyze each block of the Hughes diagram of the fiber optic phased array transmitter, and **c)** Analyze the antenna experimental radiation patterns from an active dual band phased array system. This includes comparing the data taken from the pattern characterization tests conducted in The Rome Laboratory (RL) RF Anechoic Chamber and RL Newport Research Facility, Tanner Hill (Short Range).

2.0 ANTENNA POLARIZATIONS

The antenna polarizations of this microwave dual band phased array transmitter is horizontal along a linear dimension for X-band, and vertical for L-band. This section is devoted to a wave polarization discussion because an antenna polarization is a wave polarization radiated by the antenna in a given direction.

A polarized electromagnetic wave consists of electric and magnetic field vectors ($E_\theta = \eta H_\phi$ for plane wave relationship) where they both lie perpendicular to each other in a single plane which is normal to the wave propagation direction, and the polarization direction is in the direction of the electric field vector. The electric vectors (incident and reflected field) of the horizontal and vertical polarization are horizontal and vertical with respect to the flat surface ground, respectively, as shown in Fig. 1. The ground can have a significant effect on antenna radiation if it is partially conducting at frequencies below UHF (ultrahigh frequency). The ground is usually a rather good conductor at frequencies below

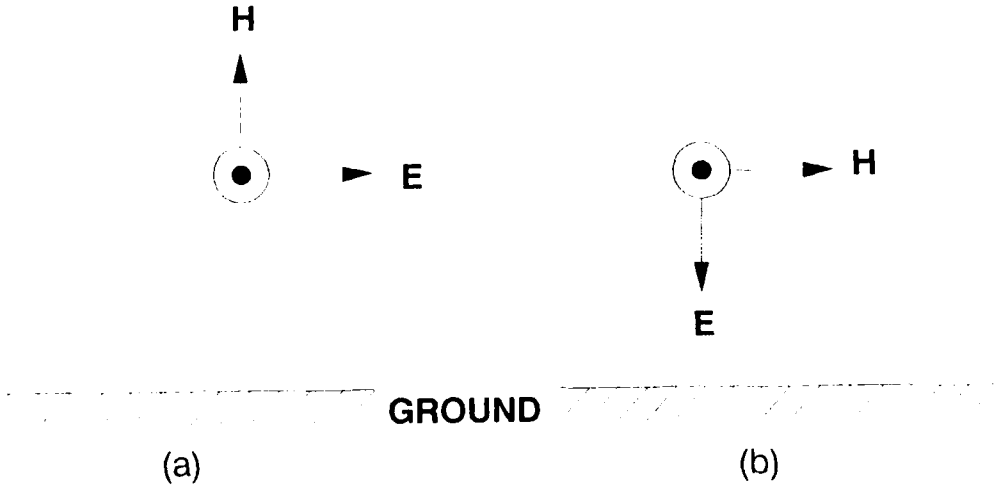

Fig. 1 Direction of linear polarization. (a) Horizontal polarization. (b) Vertical polarization.

about 10 MHz, so waves of these frequencies, over good flat surface ground, are mainly vertically polarized [7]. It also should be noted that man-made electrical noise such as energy losses in nearby houses, high-voltage transmission lines, electric motors, or power lines is mostly vertically polarized occurring below 1 GHz frequency. In addition, a low frequency operation antenna can also be effected by natural sources such as electromagnetic interferences caused by lightning, atmospheric noise, and also natural galactic and solar noise. On the other side of the spectrum, the microwave signal is severely attenuated by atmospheric absorption and precipitation at frequencies above 10 GHz [8]. Therefore a horizontal polarization should be considered for air-to-air transmission at frequencies below the UHF range in order to minimize unwanted signals that are inserted somewhere between transmission and reception. But don't short change the vertically polarized field. There are a number of applications which call for vertical polarization including air to saltwater and air to ground radar measurement that are normally conducted by using low frequency radar transmission. The disadvantage of low frequency transmission is poor efficiency. On the other hand, high frequency transmission will provide a high efficiency and large bandwidth because a bandwidth is equal to x% of a frequency response, and x is usually much much less than 1 ($x << 1$). A vertically polarized electric field tends to tilt forward over partially conducting ground causing a high energy loss in the ground. The losses can be minimized by installing metal screens or meshes on the surface of the ground in the path of antenna radiation propagation as shown in Fig. 11b. This technique can be viewed as simulating a perfectly conducting surface ground which is especially required in an experimental study of surface-to-surface transmission. The parallel combination of the imperfect conducting ground surface impedance (Z_g) and the ground screen intrinsic impedance (Z_s) helps to minimize radiation impedance (Z_r) because the impedance of the ground screen (Z_s) is much lower than the impedance of the ground (Z_g) itself. Therefore net value of Z_r can be determined by equation 1 as shown below [1]:

$$Z_r = \frac{Z_s Z_g}{Z_s + Z_g} \approx Z_s \qquad (1)$$

In addition to the ground losses, the field intensity of both linearly polarized waves is also

attenuated by intrinsic impedance of the medium (the ratio of electric over magnetic field, $\eta = E_\theta / H_\phi$) that is experienced by the propagating wave. The intrinsic impedance of air or free space $\eta_o \approx 377\Omega$ ($\approx 120\pi$).

The linearly propagating wave not only experiences ground absorption but also ground reflection. The ground usually behaves like a perfect conductor for horizontally polarized electric field [2]. Therefore, the field experiences somewhat total reflection, but its phase will be 180° out of phase with respect to the incident wave (the explanation can be made by exploring the boundary condition problems). On the other hand, ground becomes an imperfect conductor for vertically polarized electric field, and its characteristics are changed from location to location. The change is not only limited to the amplitude but also the phase.

The typical ground-reflection coefficients for horizontal and vertical polarizations are illustrated in Reference Data for Radio Engineers, 5th Edition, ITT. These coefficients are reproduced in this report to elucidate the effect of the ground, as shown in Fig. 2. The reflection coefficient of a horizontally polarized field is much greater than a vertically polarized field. The vertically polarized reflection at first decreases monotonically with decreasing incident angle until it equals the Brewster angle at approximately 85°, and then it increases concavely downward as the incident angle decreases to zero. The Brewster angle is defined as follows [3]:

$$\tan(\psi_b) = \frac{N_2}{N_1} \tag{2}$$

where ψ_b is the Brewster angle.

N_1 and N_2 are refractive indices of optically rare and optically dense medium ($N_1 < N_2$) respectively.

The Brewster angle can be derived from Snell's Law ($N_1 \sin\psi_1 = N_2 \sin\psi_2$) under the condition $\psi_1 + \psi_2 = 90°$ (ψ_1 is an incident angle), this implies that $\sin\psi_1 = \cos\psi_2$ and $\sin\psi_2 = \cos\psi_1$ [3].

If a wave is incident from a high refractive index to a low refractive index medium ($N_1 > N_2$) and $\psi_2 = 90°$ (where ψ_1 is an incident angle) then the egression wave grazes along a common surface of the two mediums (it is neither refractive nor reflective). In this case,

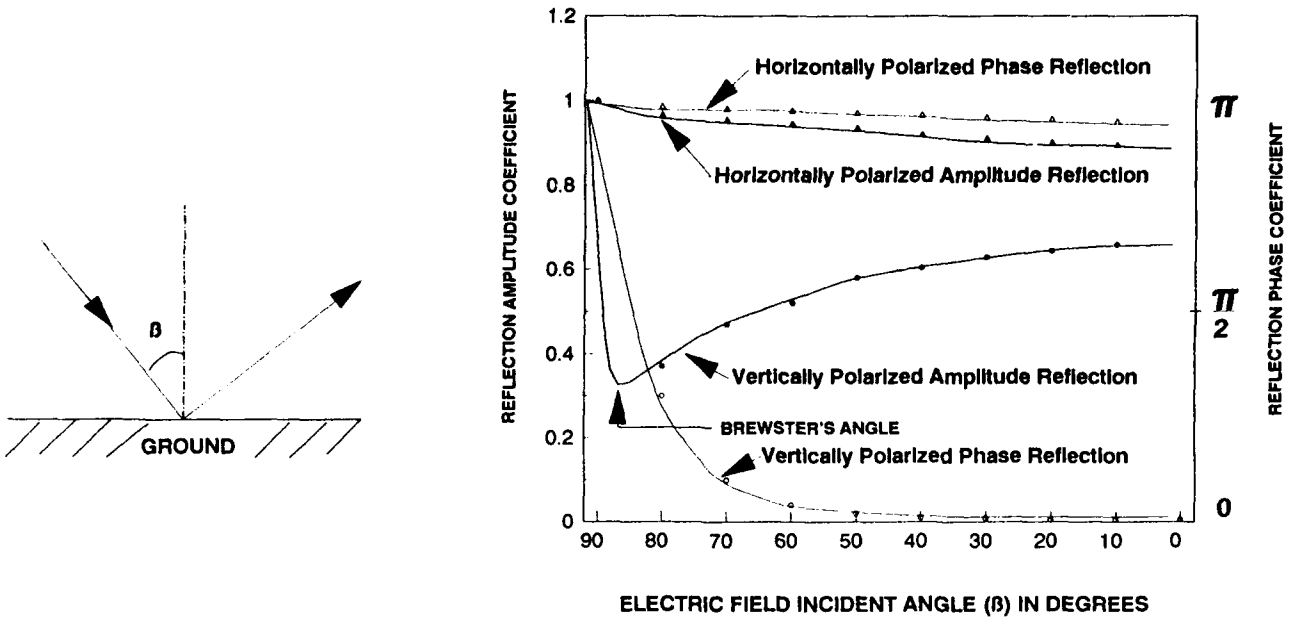

Fig. 2. Typical ground-reflection coefficients for horizontal and vertical polarizations.

an incident angle is referred to as the critical angle (ψ_c), and it can again be derived directly from the Snell's Law as shown in equation 3 below[3]:

$$\sin(\psi_c) = \frac{N_2}{N_1} \tag{3}$$

Note, if $\psi_1 > \psi_c$ then the wave is totally reflected.

if $\psi_1 < \psi_c$ then the wave is not only refracted but also reflected.

if $\psi_1 = \psi_c$ then the wave is reflected and also grazes along the surface.

A high operating frequency antenna will secure a radiation pattern from man-made noises, natural noises and ground affect (reflection and absorption) because it is not only energy loss that becomes smaller and smaller, but also the noise amplitude decreases with increasing frequency. Therefore, ground affect and noise are not major considerations for a linearly polarized high frequency antenna design.

The terms horizontal and vertical are defined with respect to the earth. These terms would be meaningless in space because the reference no longer exists. Therefore, a circularly polarized antenna is the most suitable application for space communications. The circular polarity can be visualized as two linearly polarized electric fields propagated perpendicularly. The electric field vectors rotate around in a circular path. These vectors have an uniform amplitude (no amplitude deviation) and 90° phase difference. It should be kept in mind that there is no oscillation frequency deviation between these two vectors. The circular polarization is the special case of elliptical polarization. The elliptical polarization will occur if the propagation wave consists of two perpendicularly unequal amplitudes (90° out-of-phase) between horizontal and vertical linearly polarized waves of the same oscillation frequency. Note that a linearly polarized electric field is in-phase radiation, it can be viewed as 0° out-of-phase or a collapsed ellipse. So it is also a special case of elliptical polarization. The mathematical representation of the instantaneous electric field of an elliptically polarized wave can be expressed as follows:

$$\mathcal{E}(r,t) = E_1\cos(\omega t - Kr)u_1 + E_2\cos(\omega t - Kr + \delta)u_2 \qquad (4)$$

where u_1 and u_2 are constant unit vectors ($u_1 \bullet u_2 = 0$, and $u_1 \bullet u_1 = u_2 \bullet u_2 = 1$), r is the wave propagating direction and K is a constant wave vector, ω is an oscillation frequency and t is an instant time, δ is a differential phase by which u_2-component leads u_1-component, and E_1 and E_2 are amplitude components of the electric field vectors. The polarization wave is specified at a fixed point in space (r is constant) at time t.

If δ is equal to 0 or a multiple of π, then equation (4) becomes the instantaneous electric field of a linearly polarized wave. If δ is equal to $\pm \pi/2$ and $|E_1| = |E_2|$ then equation (4) becomes the instantaneous electric field of a circularly polarized wave. Otherwise the wave will be elliptically polarized if any part of the above conditions are not true. For instance, the wave is elliptical polarization with $|E_1| = |E_2|$ and $\delta \neq 0, \pm \pi/2, \pi$ or $|E_1| \neq |E_2|$ and $\delta = \pm \pi/2$.

According to the convention, the counterclockwise rotation ($\delta = -90°$) is called right-hand polarized and the clockwise rotation ($\delta = +90°$) is called left-hand polarized. The rule of

thumb for right-hand polarization is extending a right hand thumb in the direction of propagation and curl the fingers in the direction of the rotation of the instantaneous electric field. The rule of thumb also applies to the left-hand polarization. This can be achieved by using the left hand instead of right hand. The rule is extending the left hand thumb in the direction of propagation and curl the fingers in the direction of the rotation of the instantaneous electric field [4]. It is imperative to have a polarity matched system because a receiving gain power is proportional to a polarization efficiency (polarization mismatch factor). The polarity of propagation wave and received antenna should be comparable. If a system has polarity mismatch then a polarization efficiency will be extremely attenuated. It becomes zero under orthonormal conditions. Vectors P_i and P_j in a mutually orthogonal mode are said to be orthonormal if each P_i is orthogonal to P_j (i.e. $P_i \bullet P_j = 0$ if $i \neq j$). The orthonormal in this case can be defined as an incidence of a horizontally polarized electric vector upon a vertically polarized receiver or circularly polarized counterclockwise rotation field upon circularly polarized clockwise rotation receiver, or vice versa. Notice that an incidence of any linearly polarized wave on any circularly polarized antenna (or vice versa) will reduce received power by one-half or 3 dB [4]. This technique is usually applied when a polarized wave is severely rotated due to external interference such as Faraday rotation in the ionosphere.

A total transmitted power is defined to be a combination of radiation and ohmic power. An ohmic power is a power dissipation in an antenna due to heating losses on the antenna structure (hardware) and input impedance of the antenna. The radiation power consists of the net receiving power and radiation losses. The radiation losses is a power dissipated in the transmission due to a polarization mismatch and an undiscovered power dissipation after it leaves the antenna. The polarization mismatch can cause polarization efficiency to be less than unity (it varies from 0 to 1 in value), and in turn will reduce the radiation power. The undiscovered power dissipation in space can not be retrieved, whereas power losses due to the polarization mismatch can be improved by using a polarization tracking system for polarized alignment or dissipate the 3-dB signal constantly as shown in the linear-to-circularly polarized technique.

3.0 TRUE TIME DELAY PHASED ARRAY ANTENNA RADIATION PATTERN

Two different types of linear radiation elements were used in designing the microwave multiband phased array antenna; a vertical monopole element for L-band and a dipole element for X band. A dipole element can be visualized as two point charges (q and -q) because all positive charges tend to accumulate at one end of the radiation element and negative charges usually accumulate at the other end. A monopole can be visualized as a half dipole with the use of a ground plane or any large solid metal sheet relative to the antenna size as a reference for its center feed point. A monopole calculation can easily be done by employing the principle of image theory. Note that an input voltage, input radiation impedance, radiated power, antenna beam solid angle and directivity of monopole are only half of their counterpart dipole respectively, but the current is the same for both poles [4].

In an array antenna, linearity is referred to as a straight-line geometrical configuration of the radiation element. A radiation pattern of the linear array is a function of geometrical pattern and phase factor, and the pattern known as array factor (AF). AF is a radiation field pattern of electric field radiating from excited array elements. It can be shown that the electric field ($E \propto A(r)$) is proportional to a vector potential ($A(r) \propto \int(I(z')/4\pi R)e^{-jKR}dz'$) where the amplitude and phase of A(r) are not a function of time. The amplitude of the radiating field due to each excited source is essentially the same. However, the phase is varied according to the propagation path length. Note that the phase of A(r) is $r = R + d\cos\theta$ as shown in Fig. 3, where R is a far field constant propagation path length, and $d\cos\theta$ is a far field path length difference between any two adjacent linear elements. If a uniformly excited source ($Ae^{-i\omega t}$) is applied to a laser, then the RF output signal of a photodiode in an optical true time delay module becomes $Be^{-j\omega(t+\Delta t)}$. Due to an attenuation in the transmission, B will be less than A. A and B are an amplitude signal and Δt is a fiber optic differential time delay as shown in Fig. 6. It is imperative to have equidistance (d) between any two adjacent radiating elements in the array and uniformly excited sources (constant current amplitude (I) distribution and linear phase progression) for the sake of simplicity. If the above conditions are met in an N-element module then the array factor can be expressed as follows:

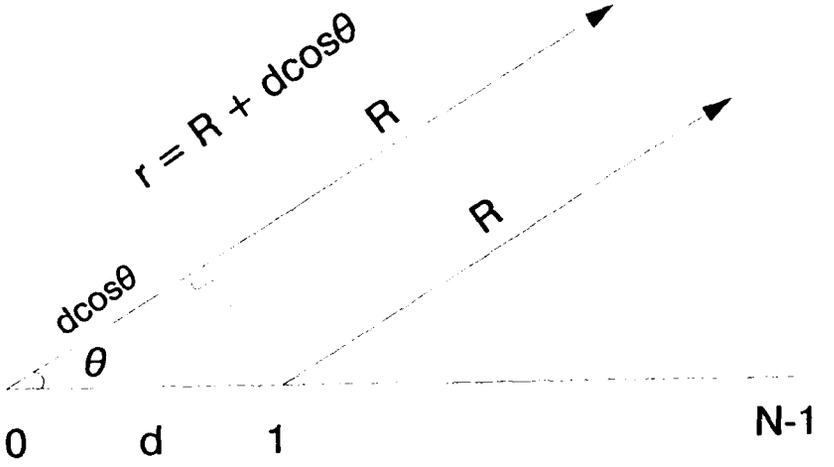

Fig. 3 Equispaced linear array isotropic radiators.

$$AF = I_0 e^{-j(\omega t + Kr)} \sum_{n=0}^{N-1} e^{jn(Kd\cos\theta - \omega\Delta t)} \tag{5}$$

It can be easily shown that equation (5) is a geometric series. With a clever maneuver, it is possible to obtain a simple formula for this expression. First multiply Eq. (5) by $e^{j\alpha}$, where $\alpha = Kd\cos\theta - \omega\Delta t$, to obtain

$$(e^{j\alpha})\, AF = I_o e^{-j(\omega t + Kr)} \sum_{n=0}^{N-1} e^{j(n\alpha + \alpha)} \tag{A}$$

Subtracting Eq. (A) from Eq. (5) gives

$$(1 - e^{j\alpha}) \bullet AF = I_0 e^{-j(\omega t + Kr)}(1 - e^{jN\alpha})$$

Solving for AF to obtain

$$AF = I_o e^{-j(\omega t + Kr)} \frac{1 - e^{jN\alpha}}{1 - e^{j\alpha}}$$

Finally, using the trigonometric Euler identity ($\sin\beta = (e^{j\beta} - e^{-j\beta})/2j$), AF can be rewritten in a more convenient form as shown in equation (6). The cofactor 1/N is a normalized amplitude of equation (6). This amplitude can be determined as follows :
Starting with $\xi = Kd\cos\theta - \omega\Delta t - (\omega t + Kr)$, then Eq. (5) is maximum when $\xi = 0$.

$$AF(\xi = 0) = I_o(1+1+1+1.....+1) = I_o N$$

The amplitude of AF is normalized to unity, i.e, $AF(\xi = 0) = 1$.
Then,

$$I_o = 1/N$$

Therefore,

$$AF = e^{j[-\omega(t+\frac{1}{2}(N-1)\Delta t)+K(\frac{1}{2}(N-1)d\cos\theta - r)]} \frac{\sin[\frac{N}{2}(Kd\cos\theta - \omega\Delta t)]}{N\sin[\frac{1}{2}(Kd\cos\theta - \omega\Delta t)]} \quad (6)$$

The optimum AF occurs when the phase factor ($e^{j\Psi}$) becomes unity, where the phase $\Psi = -\omega(t + 1/2(N-1)\Delta t) + K(1/2(N-1)d\cos\theta - r)$. The phase factor becomes a significant contribution to AF, if and only if, the array output signal is needed to combine with another output signal. Therefore, the optimal normalized array factor can be written as follows:

$$AF = \frac{\sin[\frac{N}{2}(Kd\cos\theta - \omega\Delta t)]}{N\sin[\frac{1}{2}(Kd\cos\theta - \omega\Delta t)]} \quad (7)$$

Equation (7) has clearly demonstrated the advantage of true time delay beam forming and steering over a conventional phased array antenna. In a case of true time delay phased array antenna, the beam can be steered by controlling a differential delay line (ΔL). This ΔL is proportional to a differential delay time (Δt) where it must be precisely cut to have a constantly uniform incremental delay line. On the other hand, a primary steering parameter of a conventional antenna is the phase shifter ($\cos\theta_0$) which could result in beam squint (beam wanders off target). It is also interesting to note that an antenna broadside occurs when $\omega\Delta t = 0$. A broadside can be viewed as the main beam of a polar plotted antenna pattern that is maximum in a direction normal to the plane containing the radiating elements. The antenna pattern can be steered off broadside by altering a value $\omega\Delta t$ from zero. When $\omega\Delta t$ is equal to $\pm\pi$ then the main beam is in a direction parallel to the plane containing the elements. This is called endfire antenna.

The radiation patterns of a phased array antenna, displayed in Fig. 4, are a product of computer simulation of Eq. (7). The radiating elements are equally spaced and a uniformly excited linear array. The universal array pattern for the 32-element X-band (solid line) and eight-element L-band (dotted line) are plotted at broadside in Fig. 4a and by changing the incremental time delay Δt a main beam can be steered, for instance, $\pm 90°$ at 1.9 and 9.0 GHz as shown in Fig. 4b. Notice that the steering was performed independently of frequency.

It can be shown that the maximum array factor occurs when $Kd\cos\theta - \omega\Delta t = 0$ by applying L'Hopital's rule to Eq. (7). Then the corresponding value of θ for maximum array pattern can be determined by the following expression:

$$\cos\theta = \Delta tc/d \tag{8}$$

The following parameters were used to perform a simple manipulation that in turn resulted in Eq. (8). $K = \omega/c = 2\pi/\lambda$ (phase constant for a plane wave), and **c** is the speed of light in a vacuum. If $\cos\theta$ approaches maximum value (at $\theta = 0$) then an argument ($\Delta tc/d$) in equation (8) will approach unity. The equation $(\Delta tc/d)_{\mathbf{max}} = 1$ can be utilized to determine the value of Δt if d's value is known. The interelement spacing of the array is usually limited

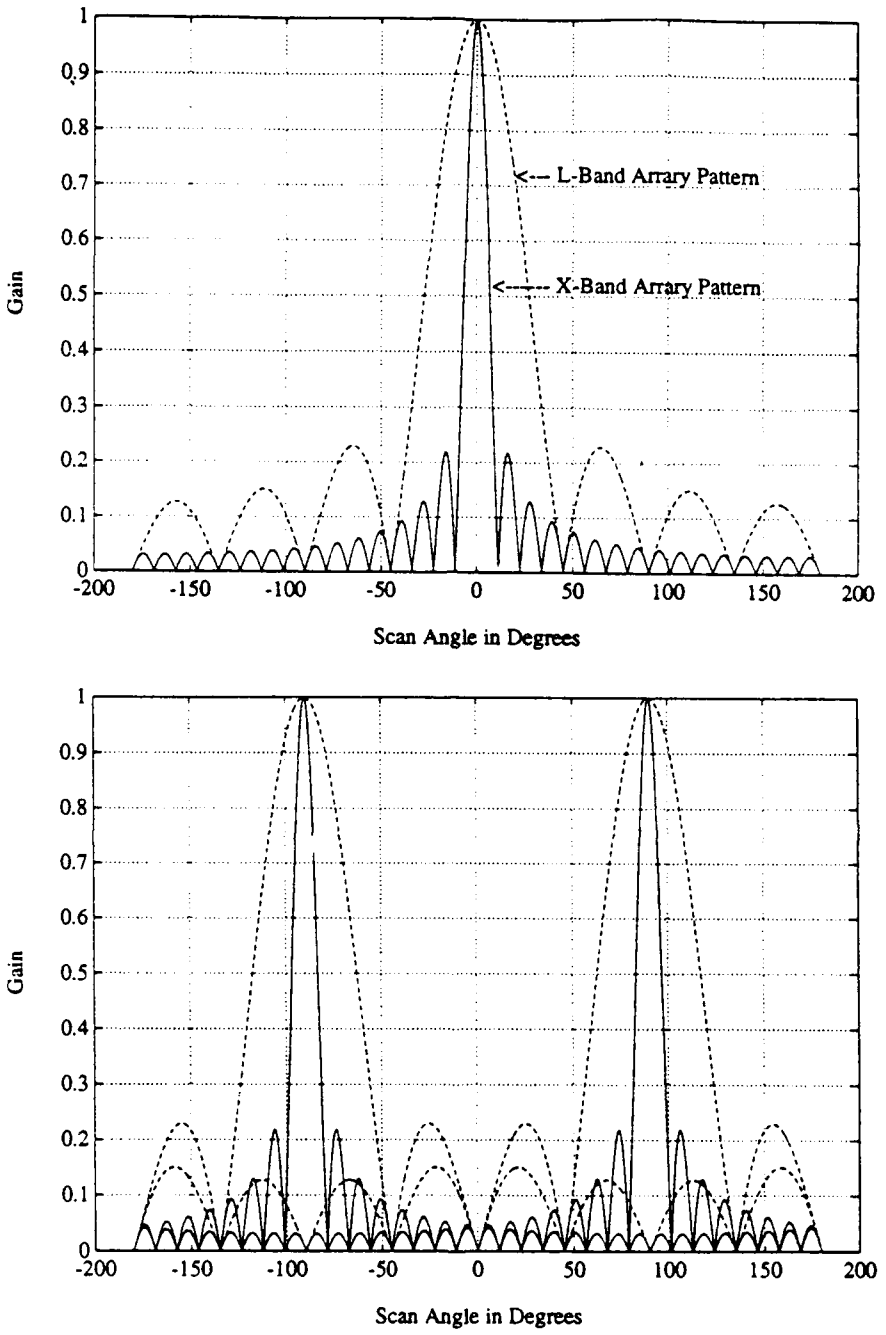

Fig. 4 Array factor of an equally spaced, uniformly excited linear array for 32-element X-band (solid line) and 8-element L-band (dotted line). (a) Radiation pattern at broadside for 1.9 and 9.0 GHz. (b) Universal pattern at $\pm 90°$ scan angles.

to a half wavelength or less ($d \leq \lambda/2$) in order to preclude multiple major lobes in undesired directions. In addition, the parameter d can also be determined by using $d = D/N$, where D is a total length of an antenna linear array and N is a number of radiating elements in the array. These two conditions will help facilitate in designing an array size and providing a precise parameter d.

Alternatively, a differential time delay Δt can also be determined if the differential RF insertion phase between the input and output ports of the delay lines in the same module is known. This differential phase is a graphical representation of the insertion phase in degrees versus frequency sweep. Picking any two points on the data plot (ϕ vs f), the difference in time delay, Δt_d, between a particular delay line and the reference (shortest) line can be calculated by utilizing the equation below [6]:

$$\Delta t_d = \left(\frac{1}{360}\right)\frac{\Delta\Phi}{\Delta f} = \frac{n_r \Delta l}{\Delta f}\left(\frac{1}{\lambda_1} - \frac{1}{\lambda_2}\right) \tag{9}$$

where $\Delta f = f_1 - f_2$ (frequency sweep) and $\Delta\Phi = \phi_1 - \phi_2$ (the differential phase). The frequency f_1 and f_2 are any two free-chosen frequency points from the differential phase plot, and in turn, the corresponding wavelengths are λ_1 and λ_2 ($f = c/\lambda$).

The value of Δt is a true time delay value, hence it will prevent the beam from wandering off target which could occur without the use of the true time delay beam forming and steering. The forming and steering of the beam can be accomplished by arranging various paths of delay lines in such a way to achieve the goal. The length of time (Eq. (10A)) and line delay (Eq. (10B)) setting for each path of each delay module can be expressed as follows:

$$t_{d,i} = t_o + i\Delta t \tag{10A}$$

$$l_{d,i} = l_o + i\Delta l \tag{10B}$$

where i = 0, 1, 2.....,(M-1)

Δt is a differential time delay

Δl is a differential fiber optic length

t_0 is a reference time delay

l_0 is a reference fiber optic delay line

$t_{d,i}$ is a true time delay of an ith path

$l_{d,i}$ is an ith path fiber optic delay line

Note that there are M delay lines in one optical delay module, and M is usually equal to 2^m where m is a bit position of a variable delay switch. Equation (10A) is often used for true time delay discussion, and the use of equation (10B) will result in a fiber optic delay line discussion. Each delay module can be used to feed more than one radiation element. However, only one line delay is needed to be active in each operation, therefore a M:1 star coupler must be deployed in each channel to achieve this performance.

Optical fiber offers a number of advantages. It is light weight, compact, wide band operation, loss is independent of frequency, and it is immune to electromagnetic interference. It is one of the prime candidates for RF true time delay applications. The velocity of signal transmission in a medium is $v = c/n_r = L/t$ therefore $c = n_r l/t$, where n_r is the refraction index of optical fiber. Thus, this equation is used to demonstrate a fundamental relationship between a fiber optic length (L) and its corresponding signal propagation time (t). Replacing c by $n_r L/t$ in equation (8), θ can be determined by the following equation:

$$\cos\theta = \frac{n_r \Delta t L}{td} \tag{11}$$

The purpose of this report is also to examine the pattern characterization tests which were not only conducted in Rome Lab RF Anechoic chamber for nearfield tests but also at RL Newport Research Facility (Tanner Hill) for far-field tests. These tests have revealed the near and far field pattern confirmation. Therefore, it is appropriate at this point to define

near and far-field regions. The parallel ray approximation begins to breakdown when the second order path length deviation is sixteenth of the wavelength. This distance is defined to be where the far field begins. The threshold of these regions can be derived from the geometry as shown in [4,5] as follows:

$$r = \frac{2D^2}{\lambda} \tag{12}$$

A near-field region is to be defined as a region having distances less than r. In order to obtain antenna radiation patterns, the distances must be equal to or greater than r. This is called the far-field region or radiation fields. And the power radiated from an antenna in the far-field region decays according to the inverse square law as a function of distance [5].

4.0 OPTICALLY CONTROLLED PHASED ARRAY TRANSMITTER

This section is devoted to an analytical description of the optically controlled phased array dual band (L and X-band) transmitter (hardware) with true time delay beamsteering as depicted in Figure 5. The operating frequencies were 1.8 to 2.0 GHz for L-band and 8.5 to 9.5 GHz for X-band. It is vital to recognize that the facts and figures in this section are based on the cooperative work and summary of Hughes final technical report (RL-TR-91-355) developed under contract to RL. The report is titled EHF Optical Fiber Based Subarrays. An RF analog input signal of both bands of the optically controlled phased array antenna will split four ways to feed four linear subarrays. The radiating elements of either band were divided into four subarrays. Therefore, four channels are needed. The divided signal in each channel will again splinter into eight throughput signals by analog fiber optic links. In other words, an analog input signal is split into thirty-two throughput signals by power dividers. There are potentially high insertion losses because a power divider is a function of amplitude. The RF input signal of both bands is 0 dBm. This signal needs to have at least 30 dB of amplification to compensate for the power divider insertion losses (which are at least 15 dB)

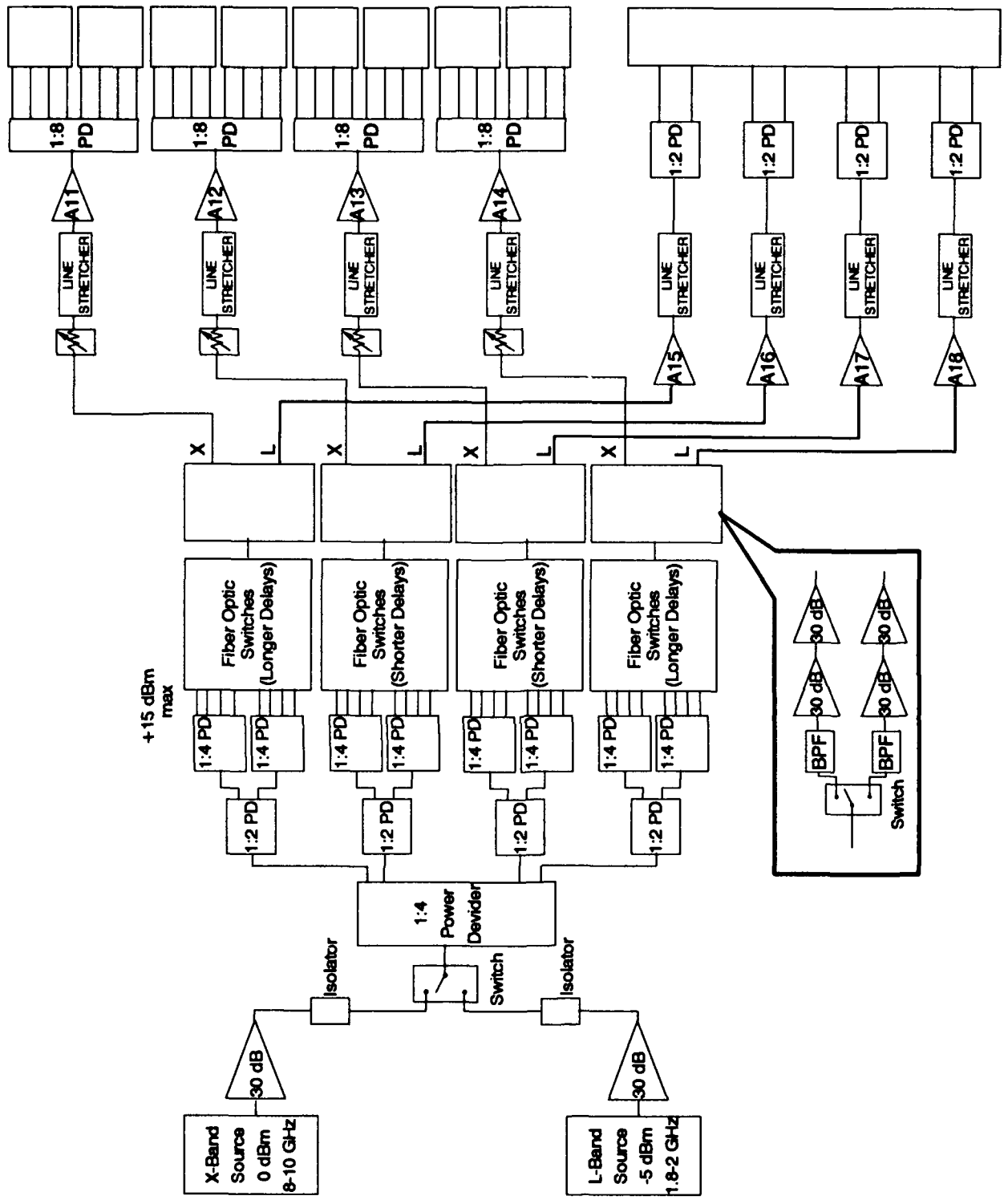

Figure 5. Optically Controlled Phased Array Dual Band Transmitter

and the fiber optic link insertion losses. The 30 dB gain custom-built preamplifiers operating at microwave frequency and a very low noise characteristic have been deployed in the transmitter. The purpose of having an RF isolator between the preamplifier and the dual bands manual switch is to prevent any feedback interference signals which can produce an unwanted intermodulation distortion through the system.

The developmental foundation of the optically controlled transmitter is solely based on a fundamental property of optic-steered phased array antennas which is the use of a fiber optic time-shifter network. This network can be precisely called fiber optic true time delay switches because the optically differential delay lines are controlled by switching on/off semiconductor lasers to provide all possible settings for beam forming and steering. Due to the resources available, the decision was made to have four sets of fiber optic switches. The time-shifter networks were arranged to have longer delay networks (channel #1 and #4) to feed the outer ends of radiating element subarrays and shorter delay networks (channel #2 and #3) to feed the two inner radiating subarrays. This arrangement will provide the proper delay values for forming a radiated phase front. The fiber optic lengths were determined by the antenna aperture and maximum steering angle, and the lengths were cut to within a 0.5 mm precision. The differential fiber optic time delay is 89 ps for channels 1 and 4 (Δt = 89 ps, Δl = 18.16 mm), and 59 ps for channels 2 and 3 (Δt = 59 ps, Δl = 12.04 mm). This transmitter was built not only for manual operation but also for computer control. Therefore, 3-bit variable switches must be used in the diode laser switching technique, which in turn provides a combination of 2^3 discrete delay increments. Therefore, four 8:1 star couplers are required in order to achieve all possible settings for beam steering. The 8:1 module is eight input fibers fused into one output fiber as shown in Fig. 6. The fiber is multimode with a refraction index of 1.47 (n_r = 1.47) and fiber dispersion of 0.2 ps/(km-nm). The eight input fibers of the star coupler are coupled to eight GaInAsP/InP buried crescent lasers operating at 1.3 μm wavelength, and one optical output is coupled to a GaInAs/InP detector with a bandwidth of about 11 GHz. The technique is called diode laser switching. Even though only one of the lasers in each delay module is activated per operation, the RF insertion loss at the output of the photodetector is still approximately 75 dB. A nonuniform insertion loss distribution of RF paths within the channel and between all channels is a valid

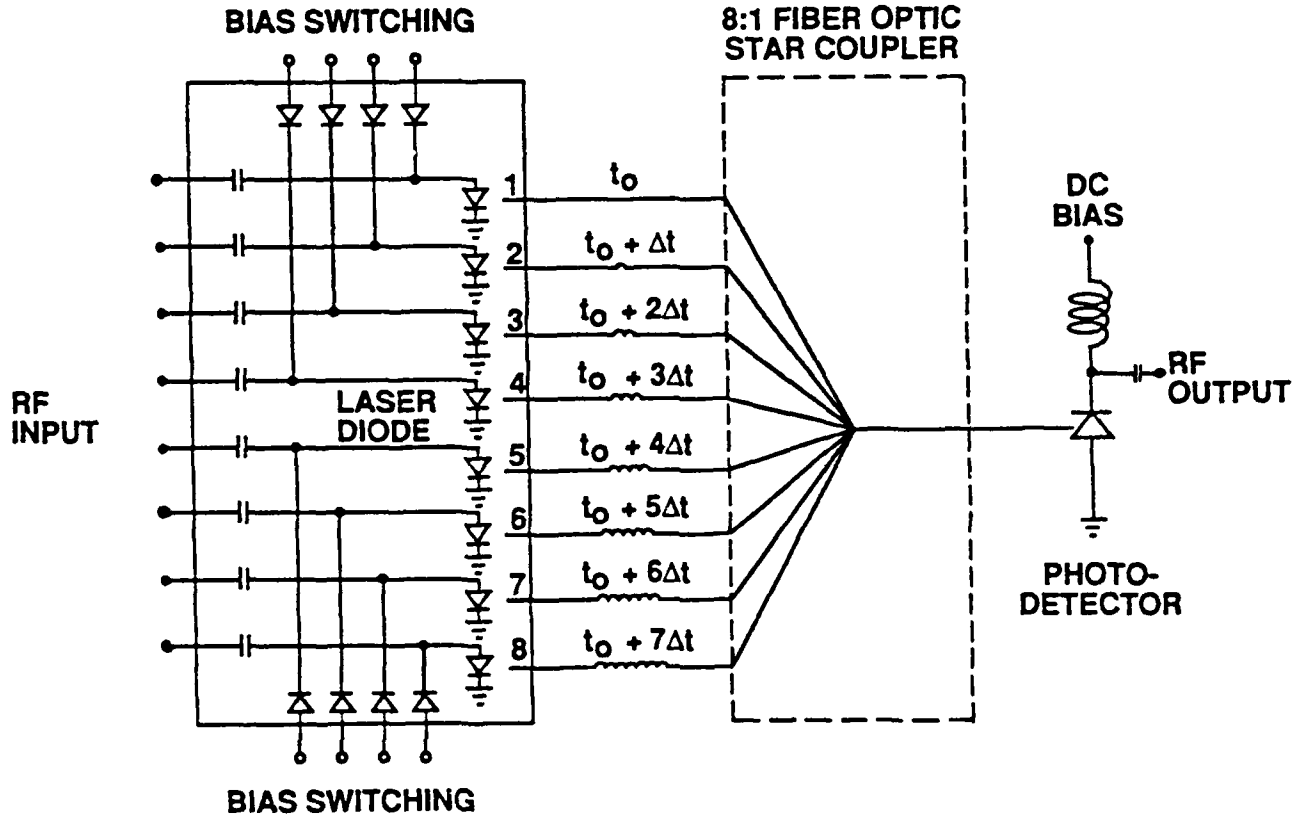

Fig. 6 Schematic diagram of 3-bit fiber optic true time delay network using semiconductor laser bias switching.

concern. Therefore, steps must be taken to ensure minimum relative lost differences. The matched performance of all four channels is crucial for the proper functioning of the beamforming. The true time delay fiber optic phase shifting of beam forming and steering can also be accomplished by the reverse operation of switching photodetectors instead of lasers. This technique is called photodetector switching. The delay module would be a 1:8 star

coupler where one input fiber splits into eight outputs coupling to detectors. There is no real distinctive advantages between the two methods, therefore, cost and availability are the decisive factors. The forming and steering of a beam to a desired angle can be accomplished independently of frequency for either technique because true time delay is independent of frequency. This process minimizes the beam squint as compared to the frequency-phase shifter operation. It is also important to recognize that both band signals share a common feed fiber optic delay network and are controlled by one set of delay lines which help to simplify the complexity of the beamforming architecture of the transmitter.

A two-bit variable switch is placed at the output of the photodiodes to allocate throughput signals to the proper bands. The photodetector's output signal on each channel will feed two radiating elements in the L-band subarray, or feed eight radiating elements in the X-band subarray. Two band pass filters (BPF), one placed in the X-band path and another in the L-band path, were used to prevent signal cross band interference. Both band signals are then introduced to 60 dB gain low noise amplifiers to compensate previous insertion losses.

The gain trimmers were used only in X-band for amplitude equalization between the channels because the angular width of each subarray falls within the angular scan limit, whereas the angular width of each L-band subarray is much larger than the maximum angular scan limit. If the amplitudes of each channel in X-band are nonuniformly distributed, it may cause a lower and wider main lobe, and in turn the side lobe amplitudes would rise. This is called destructive beamforming.

The line stretchers were required for both bands to compensate for the relative phase differences between the fiber optic beam steerer and the array system, and also between the channels. Their calibration adjustments were set to minimize errors in the system. Finally, two sets of RF low noise amplifiers with 30 dB gain for X-band and 25 dB gain for L-band were employed to bring throughput signals to the level that can be fed to the radiating element subarrays.

In this report, the words subarray and channel are used interchangeably. There are four subarrays in the system. The X-band is comprised of eight radiating elements in each subarray which are utilized to construct a baseline of 32 horizontally polarized dipole elements. There are four dipole elements in each phase-shifter module, therefore two modules are in each subarray. On the other hand, each subarray in L-band contains two vertically polarized monopoles which are used to assemble a baseline of eight radiating elements arranged side by side and lined up in a parallel structure. The linear array size of both bands is 20.8" (~ 53 cm) in length. After applying the equations $d \leq \lambda/2$ and $d = D/N$ as previously defined, the element spacing is 0.65" (~ 1.65 cm) for the X-band antenna, and 2.6" (~ 6.60 cm) for the L-band antenna. Thus the subarray size of each delay module is 5.2" ($\Gamma \approx 13.25$ cm) of both bands. The angular width, in degrees, of each subarray can be computed by $(180°/\pi)(\lambda/\Gamma)$. Consequently, each subarray angular width is approximately 15° for X-band (9.00 GHz) and 68° for L-band (1.90 GHz). This transmitter was designed for a maximum angular scan limit of ± 28° with a presetting of ±4° incremental steering angle. This design causes minimal concern for constructive beam interferences in L-band because its angular width is much larger than the maximum angular scan limit. On the other hand, the 8-element X-band subarray pattern has an angular width that falls within the angular scan limit which could cause destructive beamforming, resulting in the grating lobes becoming domineering patterns, and in turn, a mistake could be made with the main beam of the composite pattern. These errors can be corrected by using additional optical delay lines or microwave phase shifters. The decision was made to utilize phase shifters, as shown in Fig. 7, based on the resources available at the time. Also, the high insertion losses in the optical true time delay module helped influence this particular decision.

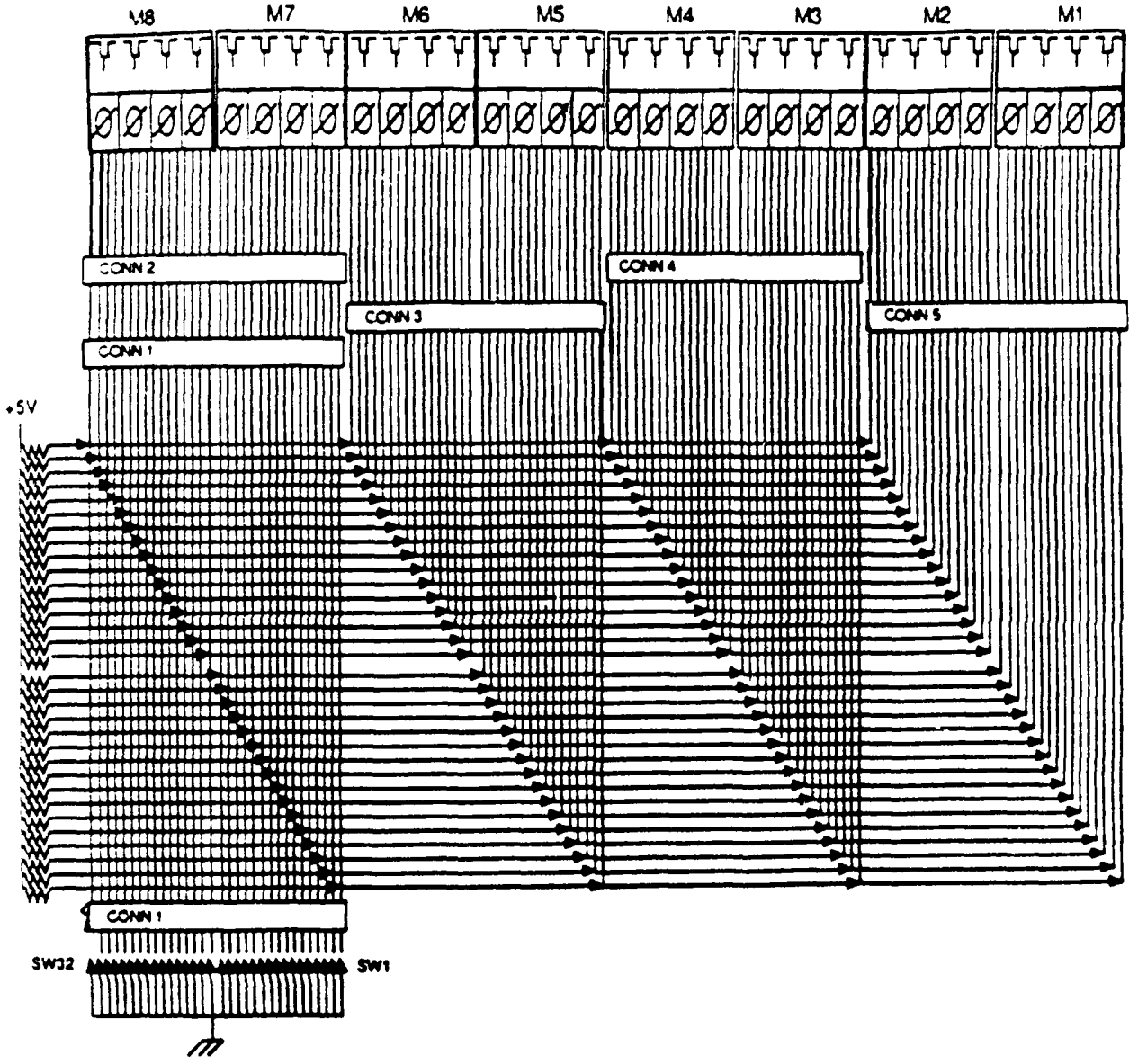

Fig. 7 Schematic of the phase shifter control unit.

5.0 ANTENNA RADIATION PATTERN

This section is devoted to the experimental analysis of the antenna radiation patterns from the active dual band phased array system. The pattern characterization tests were not only conducted in Rome Lab RF Facility Anechoic Chamber but also at the Rome Laboratory Newport Research Facility, Tanner Hill (Short Range). Equation (12) will yield the results of : R_x = 16.85 m for 9.0 GHz X-band and R_l = 3.56 m for 1.9 GHz L-band. The X and L-band receiver gain horn was mounted at 6.4 m in the chamber and at 205 m at Tanner Hill. Both measurements were taken from the transmitter to the receiver. Therefore, the pattern data from the chamber test is a near-field pattern for X-band and a far-field pattern for L-band. However, the Newport test was only to characterize radiation field pattern data of both bands in a free space environment. These experiments will be discussed in detail in the following two subsections.

5.1 ANECHOIC CHAMBER DATA ACQUISITION

The anechoic chamber is an environmentally controlled facility that can be used to determine the antenna gain, pattern data, beam pointing, and other parameters of interest in a polarization purity manner. The chamber's experimental setup including the measurement facility and instrumentation is depicted in Fig. 8a. Fig. 8b and 8c are the actual pictures of the hardware that was set up inside the anechoic chamber. The optically controlled phased array dual band radar transmitter was mounted on the rotational mount with a coordinate system defined by azimuth positioner and elevation constant. The input CW signal source to the transmitter was split, and partially distributed to a local oscillator to

perform heterodyne with a variable local frequency to establish the reference frequency at 45 MHz phase lock signal. The pyramidal horn was mounted 21 feet from the transmitter, and its receiving signal modulated with the reference phase lock local oscillator to beat down and maintain the output signal at 45 MHz for both bands. This signal was fed to a Scientific Atlanta Series 2020 Antenna Analyzer. Pattern data in hard copies were printed by the Model 1526 Rectangular Pattern Recorder.

As it has been shown previously, the signal's travelling range in the chamber experiment was near field for X-band and far field for L-band. The test was conducted at several frequencies for L-band (1.8, 1.9, 2.0 GHz) and X-band (8.5, 9.0, 9.5 GHz). The 1.9 and 9.0 GHz radiation patterns are the most appropriate representations of each band. The pattern was cut for every 4° incremental steering angle within the angular scan limit of ±28°. A cross-band boresight beam squint of 3.5° has been observed between L and X-band when the two represented frequencies were applied to the system. When performing frequency testing in each band for both bands, it has been observed that as the scan angle was steered off broadside, an error of ±2° in beam squint was observed. The cross-band squint may be due to either the calibration adjustment (line stretchers were used to perform the calibration in both bands) or radiation zone differences between L and X-band inside the chamber. The speculation that beam squint is due to the different radiating zones can be eliminated by cutting the data pattern of both bands in the radiation field. This task was conducted at **Tanner Hill**, and it will be discussed further in the following section. The 3-dB beamwidth is approximately 15° and side lobe level (SLL) is between -4 to -8.5 dB for L-band patterns, and the data patterns of X-band are approximately 5° beamwidth at 3 dB and between -5 to -15 dB relative SLL. SLL is utilized to measure how well the power is concentrated into the main lobe. It is defined as the ratio of the pattern value of the largest side lobe peak to the pattern value of the main lobe[4]. A few data patterns were chosen to represent the data patterns of both bands, as shown in Fig. 9.

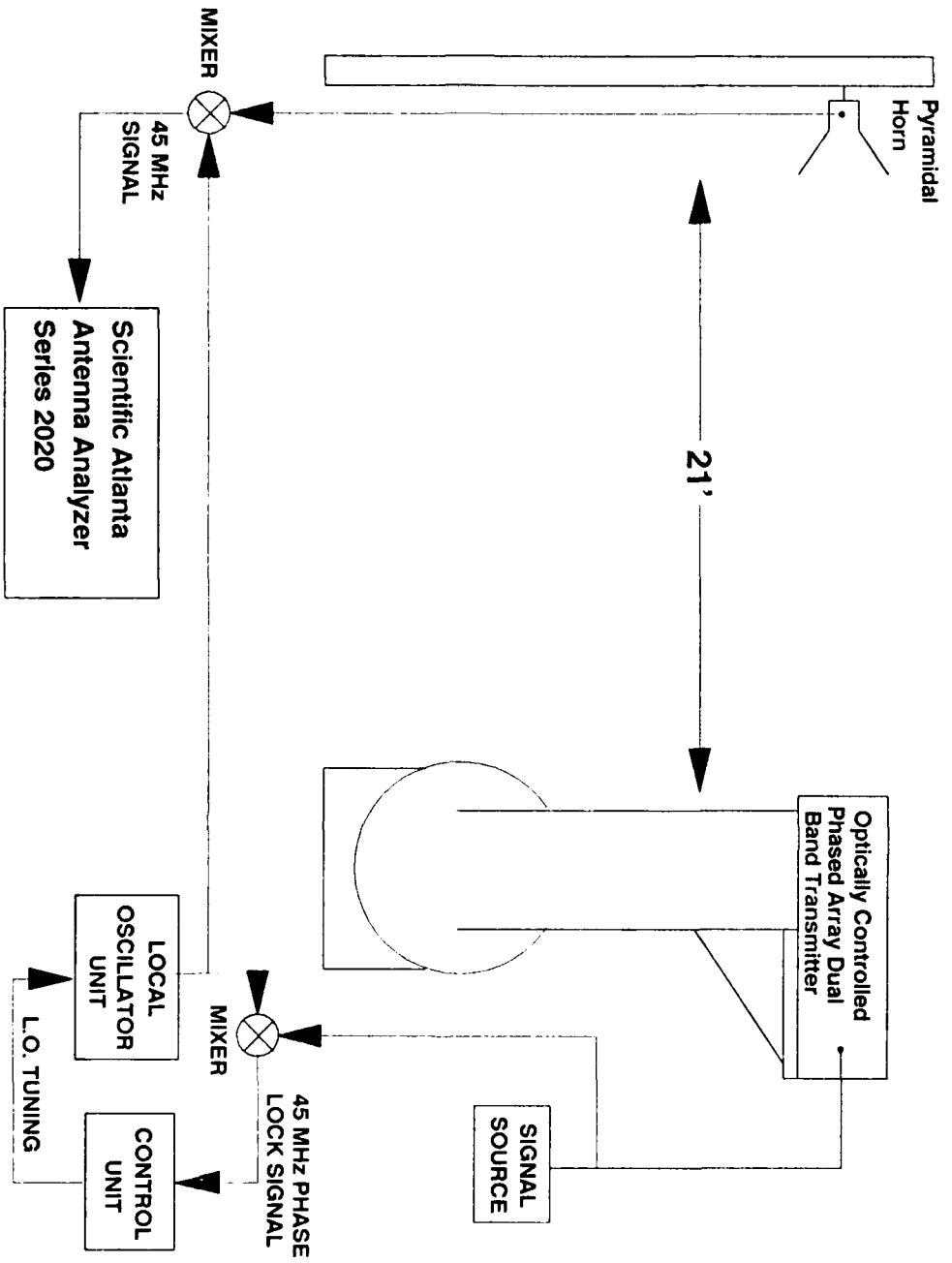

Fig. 8 The Anechoic Chamber Data Acquisition System.

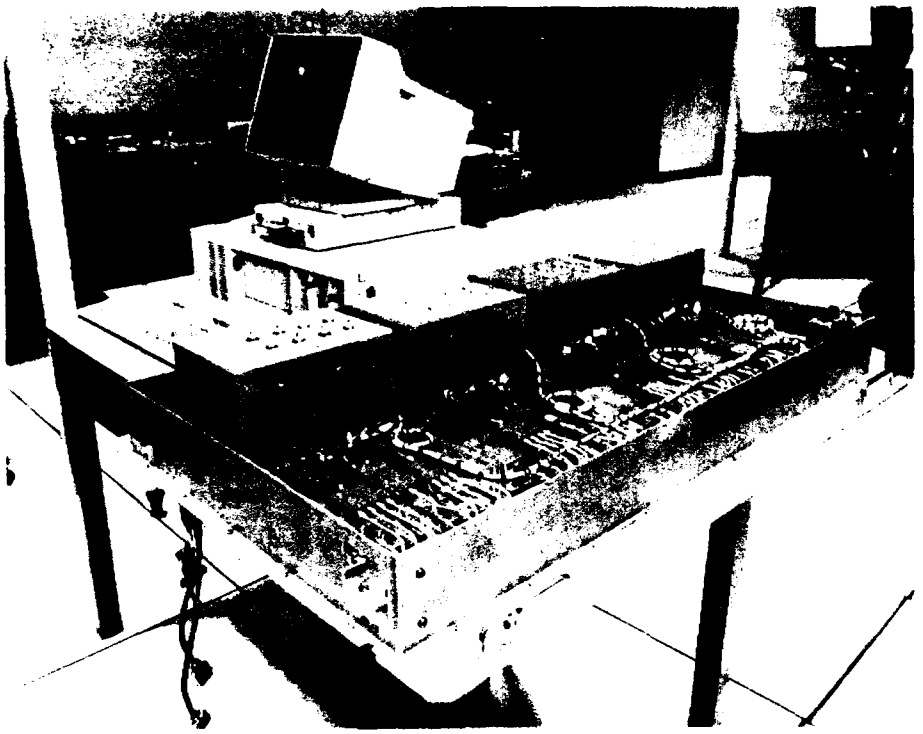

Fig. 8b Photo of 3-bit fiber optic true time delay controlled network.

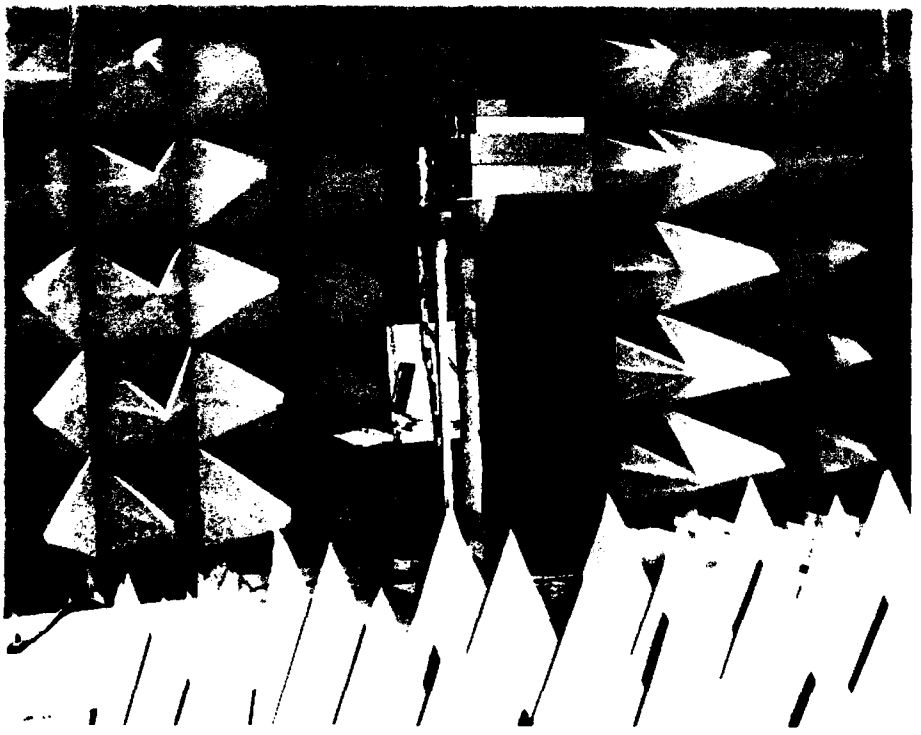

Fig. 8c Photo of optically controlled dual band radar transmitter setting up inside an Anechoic chamber.

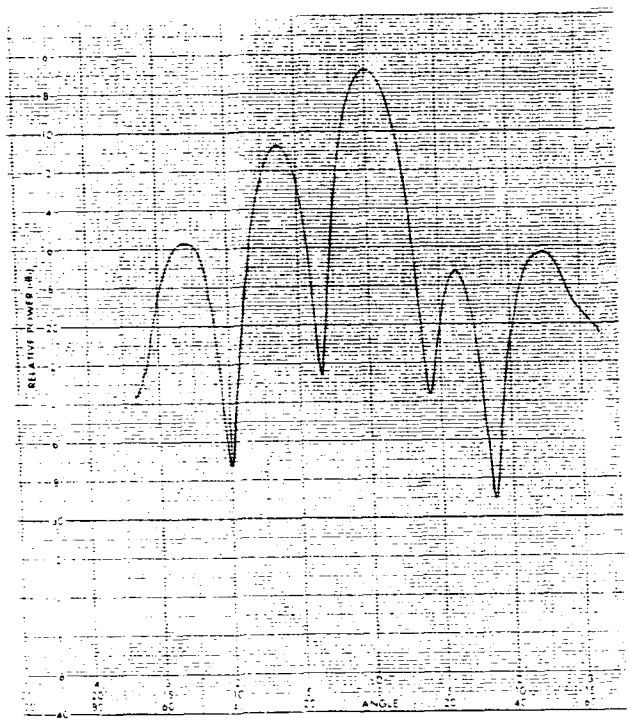

FREQUENCY: 1.9 GHz SCAN ANG: 0°

FREQUENCY: 1.9 GHz SCAN ANG: 4°

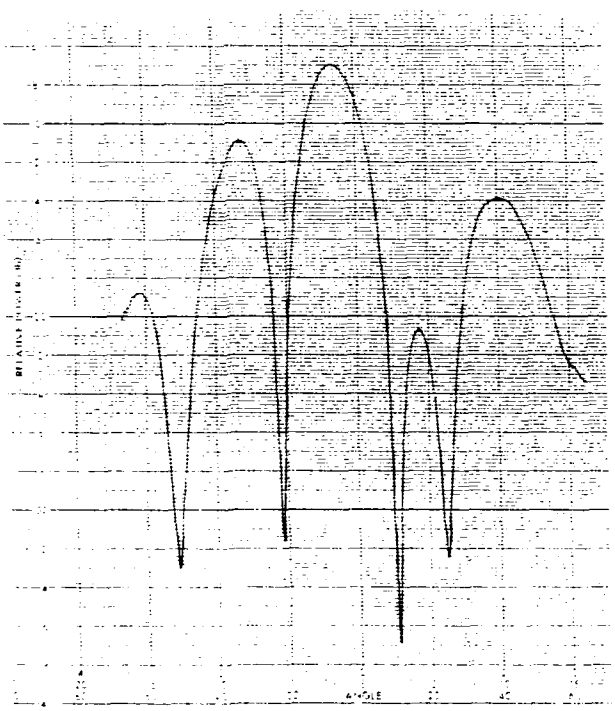

FREQUENCY: 1.9 GHz SCAN ANG: -8°

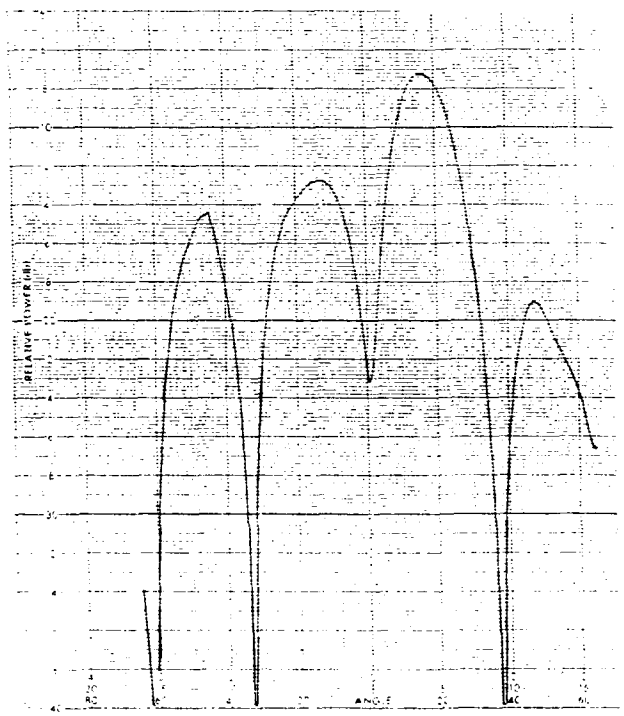

FREQUENCY: 1.9 GHz SCAN ANG: 16°

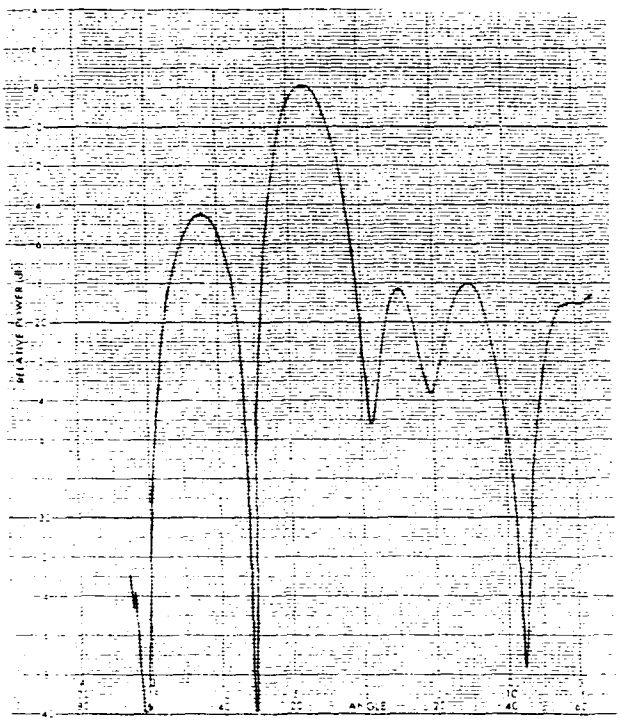

FREQUENCY: 1.9 GHz SCAN ANG: -16°

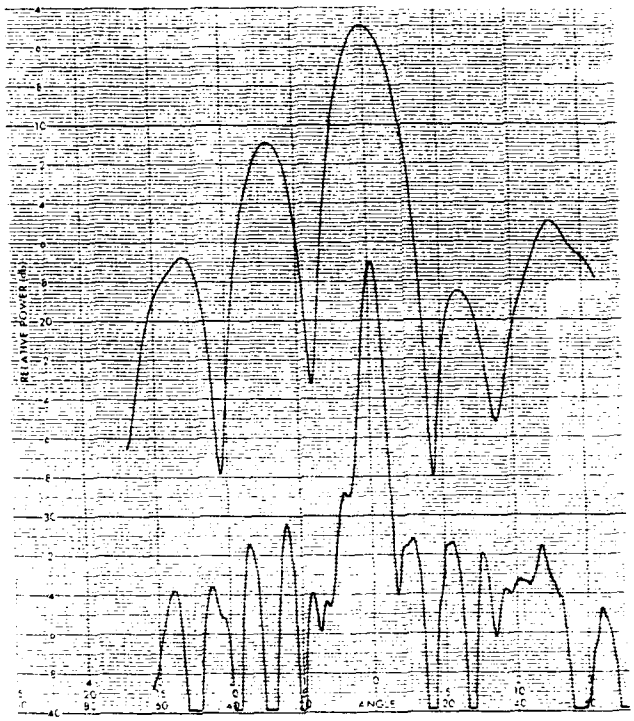

FREQ : 1.8 & 9.5 GHz SCAN ANG: 0°

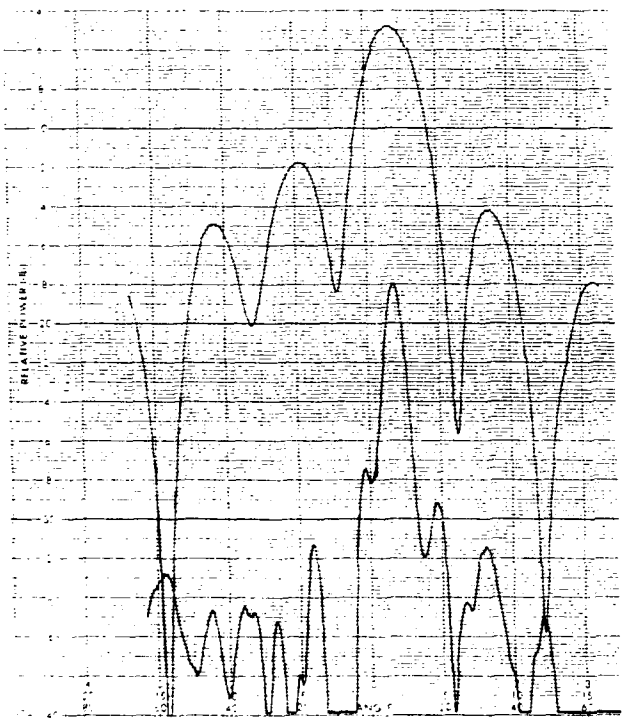

FREQ: 1.8 & 9.5 GHz SCAN ANG: +8°

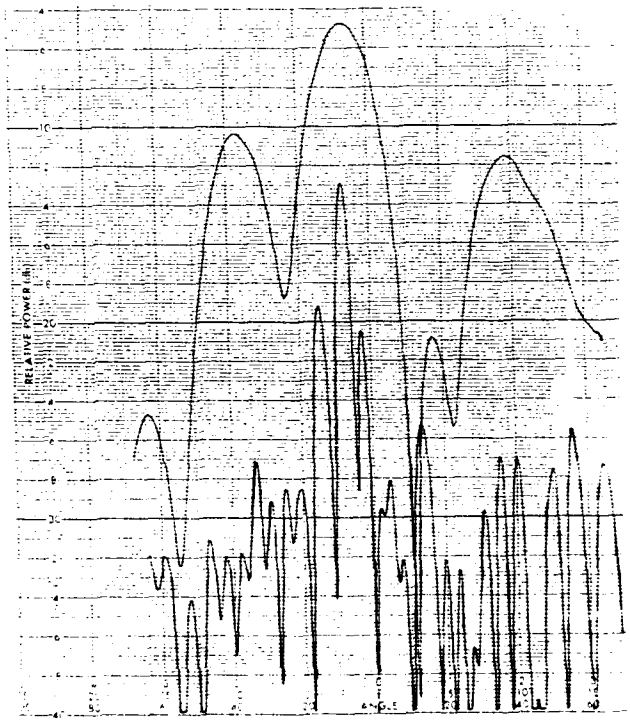

FREQ : 1.8 & 9.5 GHz SCAN ANG: -8°

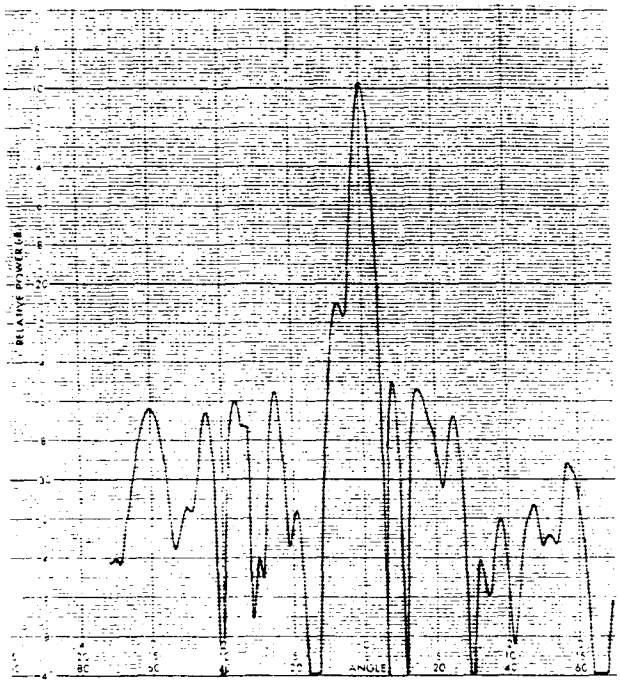

FREQUENCY: 9.0 GHz SCAN ANG: 0°

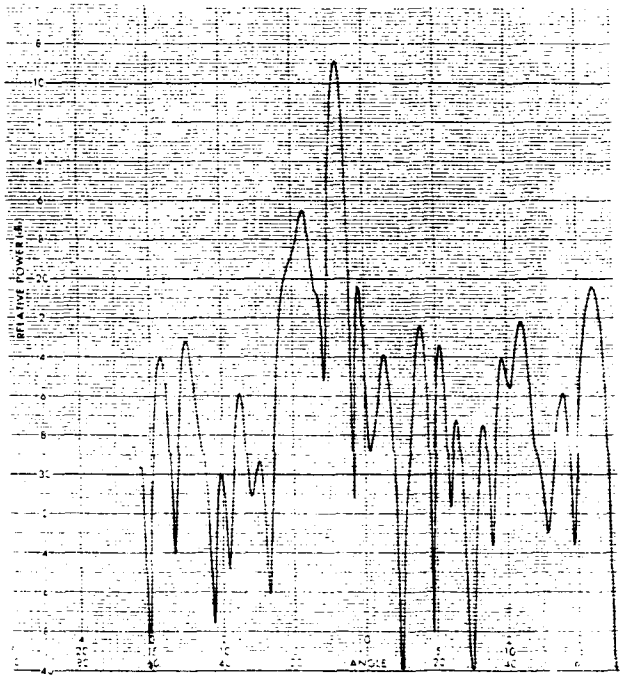

FREQUENCY: 9.0 GHz SCAN ANG: -8°

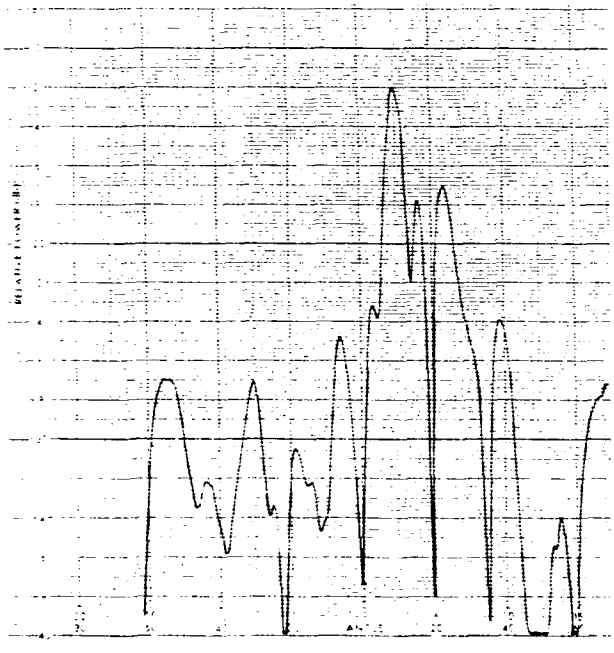

FREQUENCY: 9.0 GHz SCAN ANG: +12°

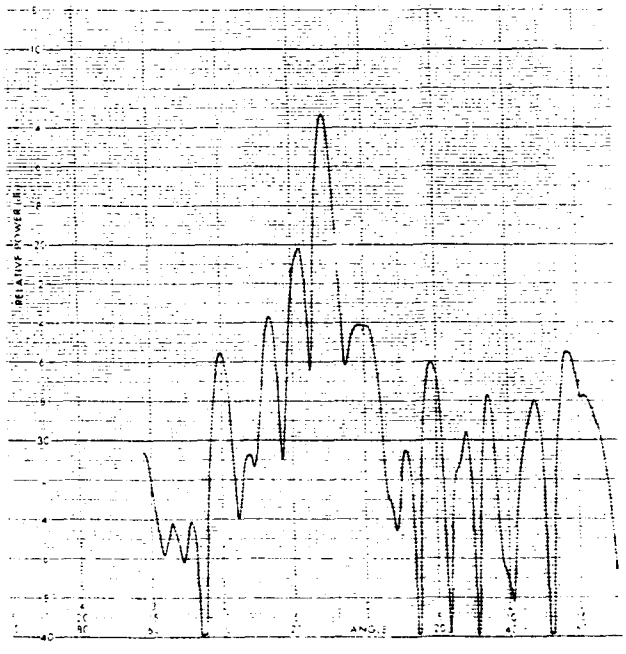

FREQUENCY: 9.0 GHz SCAN ANG: -12°

Fig. 9 Anechoic chamber radiation patterns of phased array antenna.

5.2 RADIATION FIELD DATA ACQUISITION

The objective of this section is to characterize the azimuth scanning performance of the optically controlled true time delay beam forming and steering and also to analyze its data pattern characteristics. The diagram (measurement facility and instrumentation) of the data acquisition system was set up for measuring antenna radiation pattern characteristics in a far field free space environment as shown in Fig. 10. In addition, the purpose of far-field free space test was to establish a subject for discussion. This can be done by trying to replicate the frequency and scan angle characteristics of the chamber test. These characteristics will be reintroduced here for convenient sake. These tests were conducted again at several frequencies for L-band (1.8, 1.9, 2.0 GHz) and X-band (8.5, 9.0, 9.5 GHz), with the 1.9 and 9.0 GHz radiation patterns chosen to be representative of each band. The pattern will be cut for every 4° incremental scan angle within the angular scan limit of ±28°.

The experimental setup hardware is represented in the photographs, as shown in Fig. 11. Due to the changing weather, the transmitter was placed inside a climate controlled 60" X 44" X 24" aluminum box as shown in Fig. 11a. This figure is shown with the transmitter inside the box which was mounted on top of the three axis positioner to provide a free space rotation. The transmitted signal was received by two parabolic reflectors, a 10-foot dish for L-band signal and a 2-foot dish for X-band signal, located 674 feet from the transmitter as shown in Fig. 11b. This photograph also displays the ground screen arrangement along the transmission path between the transmitter and the receiver. The dishes were mounted on polarization positioners to accomplish polarized matching with the incoming signal. The 10-foot parabolic reflector was a vertically polarized dish and the 2-foot parabolic reflector was a horizontally polarized dish. The received signal was converted into an appropriate form for data recording by a Scientific-Atlanta Precision Amplitude Receiver, Model 1780.

An HP 8340 Synthesized Signal Generator was used for both bands to provide RF signal to the antenna unit, to feed the Standard Gain Horn (SGH), and to partially distribute the signal to a local oscillator (LO), so that it could regenerate its signal to phase lock with the receive RF signal.

The purpose of SGH pattern was to verify the operation of the system. This pattern

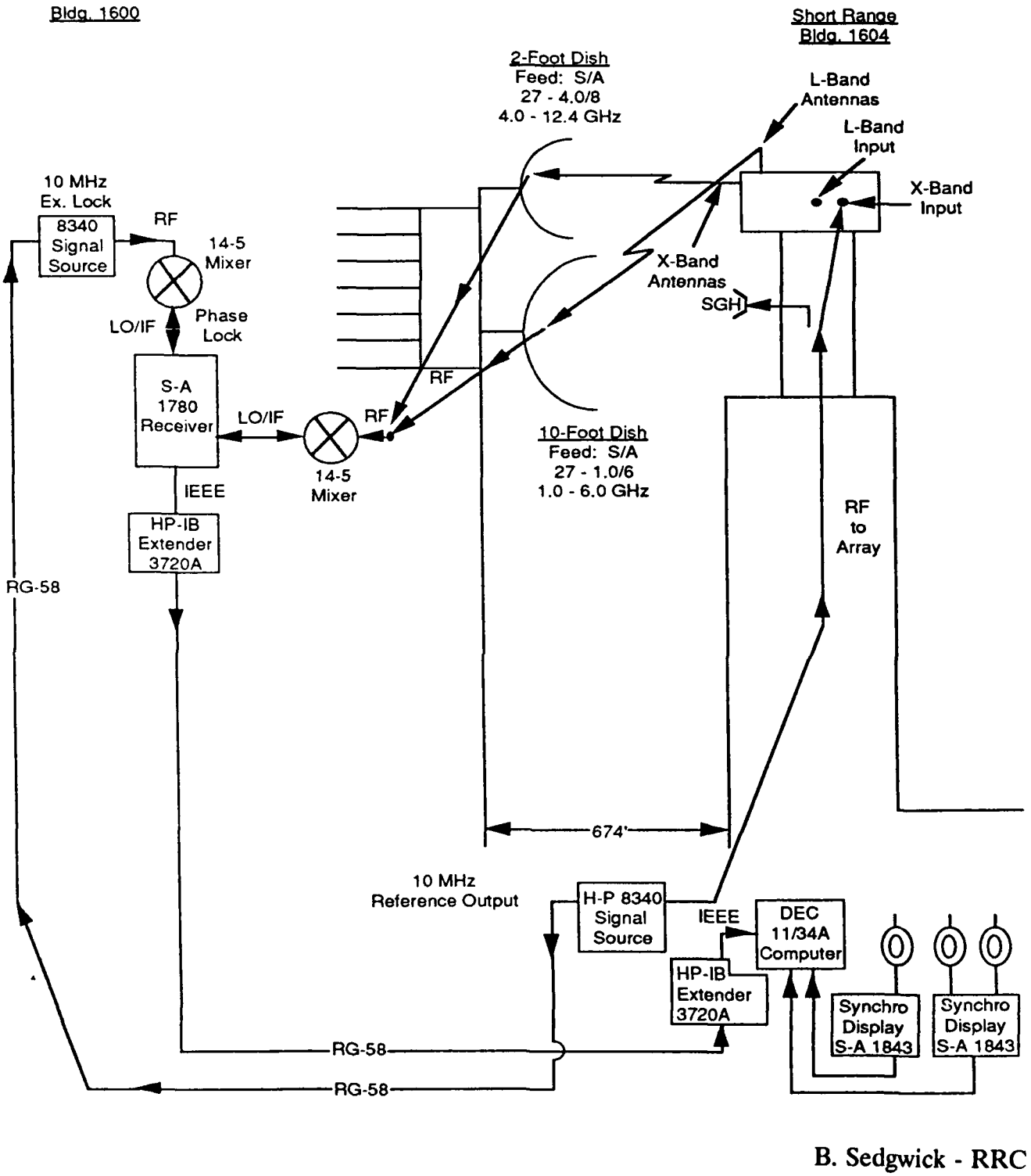

Fig. 10 Radiation field data acquisition system.

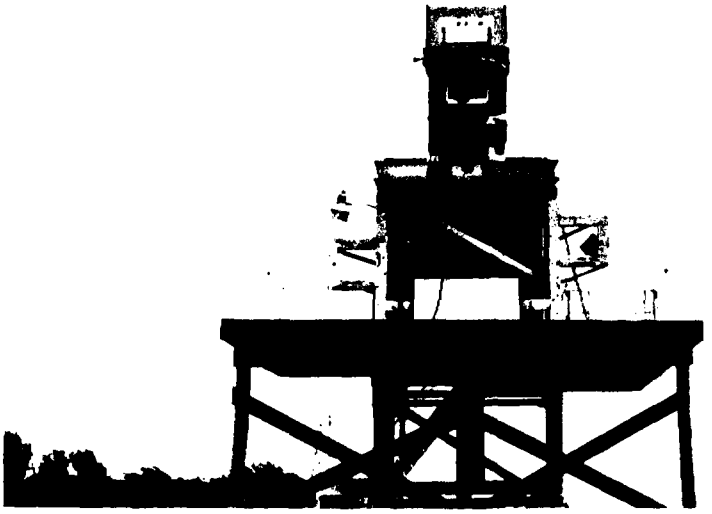

Fig. 11a Photo of true time delay phased array transmitter mounted atop the three axis positioner at the Short Range.

Fig. 11b Photo of receiving site with 2 and 10-foot parabolic receiver dishes.

was recorded at each test frequency prior to raw data recording.

The received RF signal is the output signal of the parabolic dish. The received signal was modulated with the LO signal to reproduce a 10 MHz reference output. The raw data from the radar transmitter was recorded in digital form on magnetic disk and processed at the RL Verona Research Site Data Processing and Software Development Facility, but the real-time data displayed instantaneously on a Tektronix 4014-1 Computer Display Terminal that can be used for data verification. In addition, the instant hard copies of the data pattern in rectangular plots of amplitude versus scan angle can be produced by Tektronix 4631 Hard Copy Unit.

A few data patterns from each band were chosen for the pattern representation of the far-field test as shown in Fig. 12. A crossband boresight beam squint of 3.5° between L and X-band has been observed. These tests, both in the anechoic chamber and at Tanner Hill, exhibit a constant beam squint. This confirms that the data pattern was not affected by different radiation zones. Therefore, the crossband beam squint is due to the calibration adjustment which was caused by component mismatches. The main lobes at broadside (0° scanning angle) of the different frequencies in a band stayed within 0.5° deviation of each other. In addition, in-band beam squints within 3° have been observed for each single frequency testing in each band of the L and X-band if the scanned angles were steered between ±28° by 4° increment. The beam squint is believed to be due to a slight misalignment between the antenna module within the four channels, errors in RF coaxial line lengths, and nonuniform distribution of insertion losses between all channels and RF paths. The 3-dB beamwidth and relative SLL of the L-band patterns are approximately 17° and between -3.5 to -12.0 dB, respectively. On the other hand, X-band patterns have a narrower beamwidth and higher SLL. Its 3-dB beamwidth is about 5° and SLL is between -4 to -16 dB.

The study on both sets of data patterns (controlled and free space environment) has led to the belief that changing an input frequency in each band does not significantly effect the pattern beamwidth and SLL. However, the SLL is tremendously varied by changing scan angle. The SLL is usually maximum at boresight and minimum at ±28° scan angles. In other words, the main lobe has a stronger power concentration at boresight than at off-broadside scan angles.

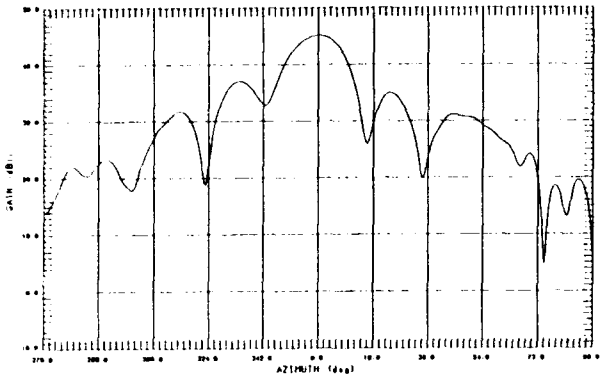

FREQUENCY: 1.9 GHz SCAN ANG: 0°

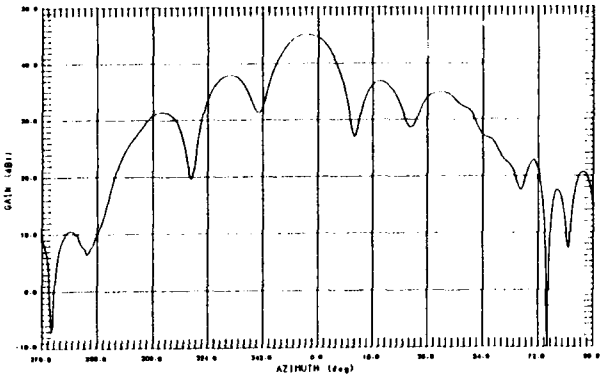

FREQUENCY: 1.9 GHz SCAN ANG: -4°

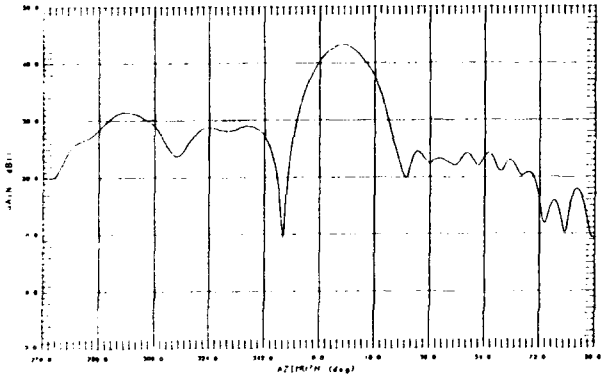

FREQUENCY: 1.9 GHz SCAN ANG: 8°

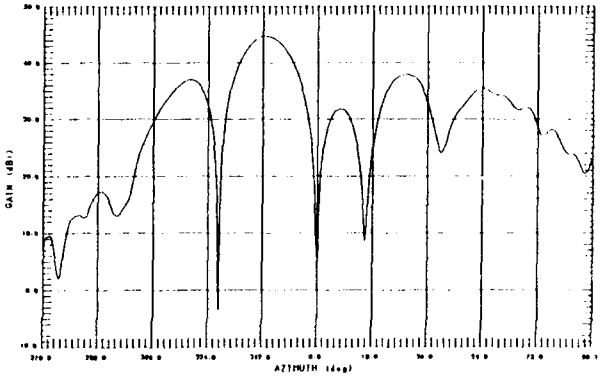

FREQUENCY: 1.9 GHz SCAN ANG: -16°

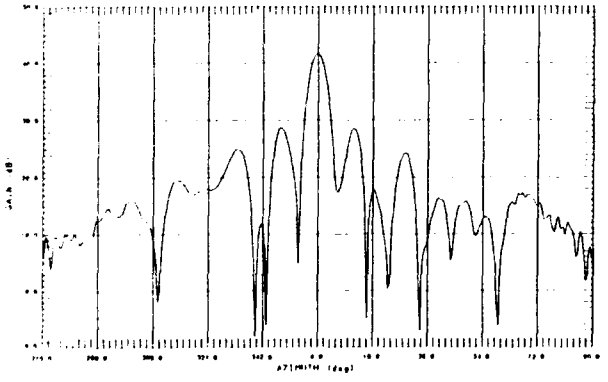

FREQUENCY: 8.5 GHz SCAN ANG: 0°

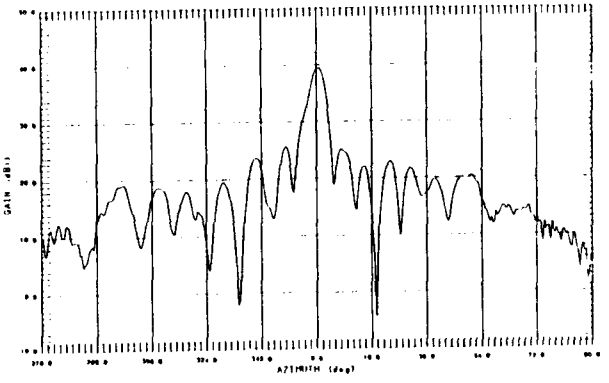

FREQUENCY : 10.0 GHz SCAN ANG: 0°

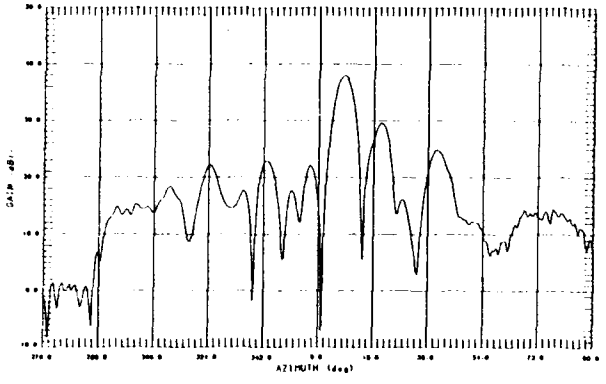

FREQUENCY: 8.5 GHz SCAN ANG: 8°

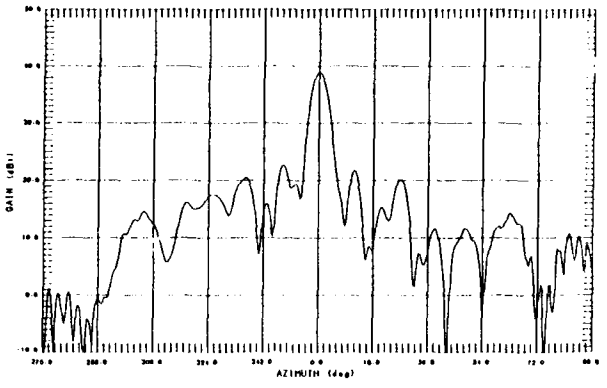

FREQUENCY: 9.0 GHz SCAN ANG: 0°

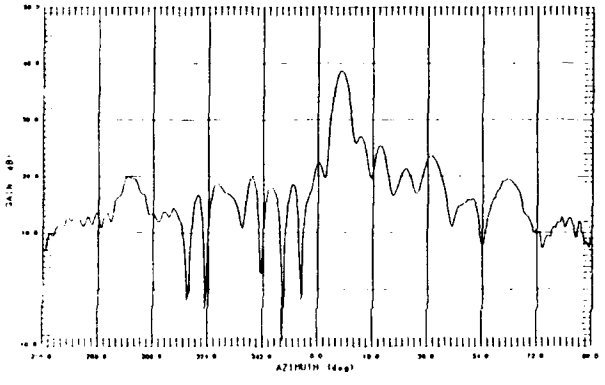

FREQUENCY: 9.0 GHz SCAN ANG: 8°

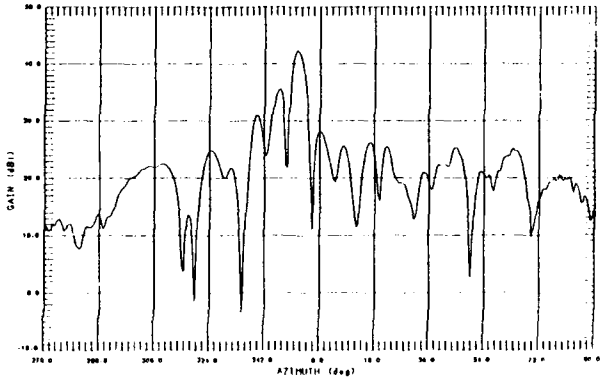

FREQUENCY: 9.0 GHz SCAN ANG: -8°

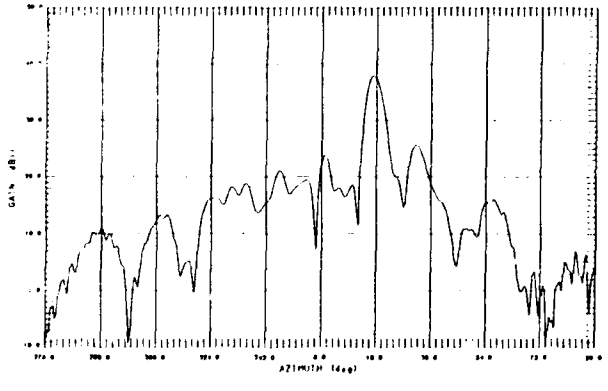

FREQUENCY: 9.0 GHz SCAN ANG: 16°

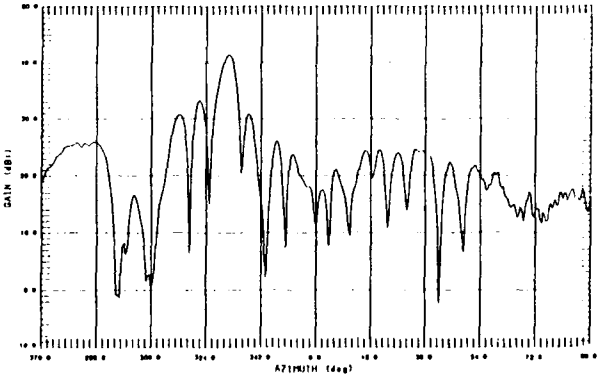

FREQUENCY: 9.0 GHz SCAN ANG: -28°

Fig. 12 Radiation patterns of phased array antenna.

5.3 ANALYTICAL DISCUSSIONS

The purpose of this section is to discuss the experimental data patterns analytically. In the preceding section it has shown that the main lobes at broadside of the different frequencies in a band stayed within 0.5° deviation of each other, and ±2° in beam squint as it was steered off broadside. These squints are partially due to the scan angle round-off error calculation, because the linear array size of 53 cm (D = 53 cm) and maximum angular scan limit of 28° (Θ = 28°) does not result in an exact 4° incremental steering angle. Since the switch is 3-bit resolution, it provides 8 discrete delay combinations. This provides a mean to compute the scan angle as follows:

If $\Lambda = D\sin\Theta$ and $\eta = D\cos\Theta$ then

$$\nabla = \frac{180°}{\pi}\left(\frac{\Lambda}{8\eta}\right) \approx 3.8° \qquad (13)$$

where ∇ is the scan angle.

The scan angle can also be found by direct calculation, that is

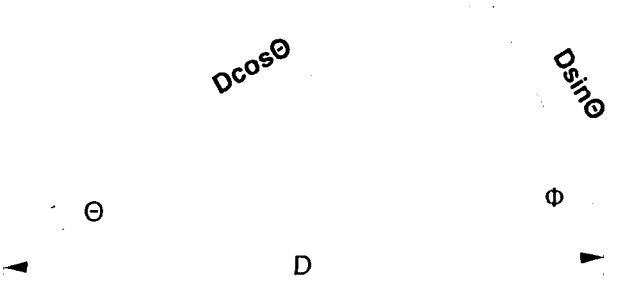

Fig. 13 Geometric composition of linear array wavefront.

$$\nabla = \Theta/8 = 3.5° \qquad (14)$$

Both approaches have confirmed that the calculated scan angle is less than 4°. Therefore, the beam squint in the same band is due to the round-off error in the calculation. This implies that this true time delay beam steering phased array transmitter exhibits high accurate beam pointing. Since the steering module is frequency independent delay lines, it is also free from beam wander off target as the frequency is changed.

It has also been observed that the crossband boresight beam squint is constantly 3.5° off set between the two bands regardless of the operating frequencies which were used in each band. The round-off errors were also partially responsible for this crossband beam squint. However, this squint is still minimum comparing to phase shifter squint. To re-emphasize this point, the theoretical analysis of phase scanning will be introduced here

to clarify any ambiguities. If phase scanning were used then the radiation electric field can be represented as follows:

$$E_i(\theta_i,t) = \sum_{n=0}^{N-1} I_n \, e^{-j(\omega t + \Psi_n - nKd\sin\theta_i)} \tag{15}$$

Note that this equation is very similar to equation (5), true time delay steering equation. It seems to be deceiving to express Eq. (5) in term of cosine and Eq. (15) in term of sine, but, as shown in Fig. 13, the sum of the two angles is 90° ($\theta + \phi = 90°$). Equation (15) was derived by looking at the overall wavefront geometry. Wavefront is defined as the plane which is perpendicular to a beam pointing direction. On the other hand, Eq. (5) was derived by observing spatial advancement of a radiation field geometry.

Let's assume Ψ_n's are fixed but frequency is now changed. If two propagation electric fields radiate with different frequencies at time t = 0 and the sources are uniformly excited then the fields are proportional to each other when the phases are equal, i.e. $\Psi_n - nK_1d\sin\theta_1 = \Psi_n - nK_2d\sin\theta_2$. After a few simple cancellations, this expression can be rewritten as follows:

$$K_1\sin\theta_1 = K_2\sin\theta_2 \tag{16}$$

This equation is called Bragg diffraction equation. Substituting $2\pi/\lambda$ for K then the equation becomes:

$$f_1\sin\theta_1 = f_2\sin\theta_2 \tag{17}$$

This is the modified Bragg diffraction equation, where f_i is a carrier frequency and θ is a scan angle. For instance, if f_1 = 1.9 GHz, $\theta_1 = 4°$, and f_2 = 9.0 GHz then, by applying Eq. (17), $\theta_2 = 0.84°$. The squint for this particular case is $\theta_1 - \theta_2 = 3.16°$. Let's again calculate the squint when $\theta_1 = 28°$ and frequencies f_1 and f_2 are constant, then $\theta_2 = 5.69°$. The squint is now $\theta_1 - \theta_2 = 22.31°$. According to Eq. (17) a crossband beam squint for the phase shifter does not exist at broadside, but it becomes broader and broader as the scan angle is steered

away from broadside. So it is undoubtedly an advantage to utilize true time delay optical beamforming and steering.

To have a valid comparison, both systems should have equispaced linear arrays that are uniformly excited with progressive phase shift between successive elements. Modify Eq. (5) to govern antenna phase scanning applications. This equation can be expressed as follows:

$$AF = I_o e^{-j(\omega t + Kr)} \sum_{n=0}^{N-1} e^{jn(Kd\cos\theta - \Delta\psi)} \quad . \tag{18}$$

A maximum of an array factor occurs when $Kd\cos\theta - \Delta\psi = 0$. Then this equation can be expressed as follows:

$$\Delta\psi = 2\pi f(d/c)\cos\theta_o \tag{19}$$

where θ_o is the corresponding angle for which the array factor is maximum, and $\Delta\psi$ is the phase delay between any two adjacent antenna elements. Equation (19) is frequency dependent, this implies that the scan angle is frequency sensitive. With a small change in the operating frequency, the beam pointing direction is also changed. In fact, phase scanning is a potential beam drifter (beam wanders off target) and phase squint in broadband beams. On the other hand, true time delay with wideband radiating elements permits large transmit and receive frequency excursions without beam wander as the frequency is changed, and also permits the use of wideband waveforms. The true time delay scanning is frequency insensitive over a wideband signal. The incremental true time delay between successive elements was derived and has shown in Eq. (8). Let's reintroduce this equation below, so it can easily be done the comparison with Eq. (19).

$$\Delta t = (d/c)\cos\theta_o \tag{20}$$

Since the scan angle θ_o is time dependent, equation (20) is frequency insensitive. It is interesting to notice that both equations (Eq. (19) and (20)) only differ by the factor $2\pi f$. All parameters in Eq. (20) are fixed which in turn should not provide any squint at all.

6.0 CONCLUDING REMARKS

The experimental pattern data of the RL Anechoic chamber and Tanner Hill have shown in-band and cross-band beam squint. The squint is believed to be due to calibration adjustment. The adjustment is to compensate for the round-off error of finite and fixed delay lines in each channel at any scan angle and for the phase round-off error within each subarray, and also for component mismatches. It is important to recognize that these beams did not randomly wander off target. In other words, there was no recognizable deviation of data pattern if the same test was repeated a number of times. There is no doubt that repeatability and predictability of the system out-weighs beam squint. The so-called beam squint is defined as the difference between calculated input scan angle and data pattern scan angle. Therefore, the squint can be minimized by an accurate calibration adjustment and an extremely precise scan angle calculation. The data confirms that the implementation of photonic beam forming and steering into an RF phased array antenna will permit frequency hopping over a wide frequency range without the resultant beam squint present, as in a conventional RF phased array antenna. Unlike a conventional antenna, the signals of the dual band optically controlled true time delay transmitter share a common feed fiber optic delay network and are controlled by one set of delay lines which help to simplify the complexity of the beamforming architecture of the antenna. In addition, the use of fiber optic delay lines in the phased array antenna instead of phase shifters has the following advantages: lightweight, compactability, flexibility, wideband operation, nondispersive over multiple bands of microwave frequencies, and immunity to electromagnetic interference. The advantage extends to both communications and surveillance applications where the beam wandering off target could occur without the use of the optically controlled true time delay beam forming and steering. This system is also suitable for spaceborne and airborne phased array applications.

REFERENCES

1. M. T. Ma, "Theory and Application of Antenna Arrays", pp. 283 - 285, New York : Wiley, 1974.

2. ITT, "Reference Data For Radio Engineers", 5th Ed. pp. 25-36 - 25-37, Indianapolis : Sams, 1968.

3. L. Bernstein, "Planar Optical Waveguides", pp. 21 - 27, Brooklyn, New York : Polytechnic University, Class Note.

4. W. L. Stutzman, G. A. Thiele, "Antenna Theory and design", pp. 13 - 31, 53 - 56, 84 - 94, 124 - 130, New York : Wiley, 1981.

5. D. Slater, "Near-Field Antenna Measurements", pp. 7 - 9, Boston : Artech House, 1991.

6. Dr. G. L. Tangonan, Dr. W. W. Ng, J. J. Lee, M. Wechsburg, "EHF Optical Fiber Based Subarrays", Hughes Research Laboratories, RL-TR-91-355, Final Technical Report, December 1991.

7. G. L. Hall, "The ARRL Antenna Book", 14th Edition, pp. 1-1 - 1-6, 2-9, 8-15, Newington, CT : The American Radio Relay League, 1984.

8 W. Stallings, "Data and Computer Communications", 2th Edition, pp. 60, New York : Macmillan, 1988.

ACKNOWLEDGEMENT

I would like to express my sincere appreciation for the many useful comments and suggestions provided by Mr. James Hunter, Rome Laboratory project engineer, and Captain Marc Robertson, US Air Force, who reviewed this technical report during the course of its development. Special thanks is also due to Norman Bernstein, Rome Laboratory project engineer, for his most gracious encouragement and technical know-how in the area of photonic subsystems.

*U.S. GOVERNMENT PRINTING OFFICE: 1993-710-093-60303

MISSION

OF

ROME LABORATORY

Rome Laboratory plans and executes an interdisciplinary program in research, development, test, and technology transition in support of Air Force Command, Control, Communications and Intelligence (C^3I) activities for all Air Force platforms. It also executes selected acquisition programs in several areas of expertise. Technical and engineering support within areas of competence is provided to ESD Program Offices (POs) and other ESD elements to perform effective acquisition of C^3I systems. In addition, Rome Laboratory's technology supports other AFSC Product Divisions, the Air Force user community, and other DOD and non-DOD agencies. Rome Laboratory maintains technical competence and research programs in areas including, but not limited to, communications, command and control, battle management, intelligence information processing, computational sciences and software producibility, wide area surveillance/sensors, signal processing, solid state sciences, photonics, electromagnetic technology, superconductivity, and electronic reliability/maintainability and testability.